Cryogenic Selective Surfaces

Final Report on a Phase I NIAC Study

February 2016

Robert C. Youngquist and Mark A. Nurge

Preface

Several years ago, a small piece of Space Shuttle Orbiter payload bay door liner was handed out to each member of the KSC workforce as a space memento. I remember studying this small piece of clear plastic with its reflective coating and wanting to understand why this was special. After some research, I soon understood that it was designed to reflect away sunlight, but still allow infrared energy to be emitted, allowing the payload bay doors of the Orbiter to radiate heat even in the presence of the Sun. I thought this was quite ingenious.

Then, a few years later, I was working on galactic cosmic radiation (GCR) active shielding methods. I looked seriously at electrostatic shielding and could not find a workable path, so I considered magnetic field shielding. Many closed toroid designs had been proposed for this purpose, but their containment structures would generate significant radiation when they interact with the GCR, bypassing the protection of the magnetic field. So I began to look at open magnetic field structures composed of long lengths (kilometers) of superconducting wire located significant distances from the spacecraft. I became convinced that this was the only practical route for protecting astronauts from GCR with an active shield, but the key problem was how to keep these wires cold so that they would stay superconducting. Prior work had assumed that the wires could be located in liquid-nitrogen sheaths, but I doubted that was practical or would even be possible.

Then, one day, I was doing some blackbody calculations for another project and decided to calculate the stable temperature of a perfect reflector covered with a material perfectly transparent in the visible and perfectly emissive in the infrared. I soon saw that if the cutoff wavelength was at 5 μm, the structure would chill to below liquid-nitrogen temperatures. So I had a solution based on ideal materials, but I was unable to find interest (i.e. funding) in this topic and I dropped it for a few more years.

Finally, I decided in 2014 to make an attempt at obtaining NIAC funding by proposing this idea, which I called cryogenic selective surfaces. I knew that there were problems with maintaining cryogens in deep space and saw that using nearly ideal selective surfaces might solve this. The fact that this idea was not well known was a bit surprising in that Hibbard from NASA Lewis suggested it in 1961, but since no one seemed to have seen the applications or potential, it was not explored. In May 2015, NIAC selected this topic for Phase I funding, though with the "suggestion" that we not consider GCR shielding and only concentrate on cryogenic maintenance. The following report details the work performed under this Phase I NIAC funding.

rcy

Executive Summary

There are many challenges involved in deep-space exploration, but several of these can be mitigated, or even solved, by the development of a coating that can reject most of the Sun's energy and yet still provide some far-infrared heat emission. Such a coating would allow non-heat-generating objects in space to reach cryogenic temperatures without using an active cooling system. This would be a benefit to deep-space sensors that require low temperatures, such as the James Webb Telescope focal plane array. It would also allow the use of superconductors in deep space, which could lead to magnetic energy storage rings, lossless power delivery, or perhaps a large-volume magnetic shield against galactic cosmic radiation. But perhaps the most significant enablement achieved from such a coating would be the long-term storage in deep space of cryogenic liquids, such as liquid oxygen (LOX).

In this report, we review the state of the art in low-temperature coatings and calculate the lowest temperatures each of these can achieve, demonstrating that cryogenic temperatures cannot be reached in deep space in this fashion. We then propose a new coating that does allow coated objects in deep space to achieve the very low temperatures required to store liquid oxygen or nitrogen. These new coatings consist of a moderately thick scattering layer (typically 5 mm) composed of a material transparent to most of the solar spectrum. This layer acts as a scatterer to the Sun's light, performing the same process as titanium dioxide in white paint in the visible. Under that layer, we place a metallic reflector, e.g. silver, to reflect long-wave radiation that is not well scattered. The result is a coating we call "Solar White," in that it scatters most of the solar spectrum just as white paint does for the visible. Our modeling of these coatings has shown that temperatures as low as 50 K can be reached for a coated object fully exposed to sunlight at 1 AU from the Sun and far from the Earth.

In the second half of the report we explore a mission application of this coating in order to show that it allows LOX to be carried on a mission to Mars. Heat can reach a LOX tank in five ways: direct radiation from the Sun, scattered or reflected radiation from the Sun off of spacecraft components, radiation from nearby planets or the Moon, radiation from the infrared emission of other parts of the spacecraft, and conduction along support struts and flow lines. We discuss these and sum their total contribution when using a Solar White coating to demonstrate an architecture that allows the transportation of LOX to Mars. After this, other applications of Solar White are listed.

Contents

Tables

Figures

1. OVERVIEW OF THE SOLAR WHITE COATING

Selective surfaces [1], also known as thermal control coatings, are often used in spacecraft applications to minimize the absorption of solar radiation, yet allow infrared (IR) energy to be emitted [2–4]. The net result of using these coatings is to allow waste heat to be radiated while minimizing the solar heat load, providing thermal control of the spacecraft. However, NASA now has a need to, not reject waste heat, but to maintain cryogenic temperatures in deep space so that cryogenic commodities can be kept cold and superconductors can operate without refrigeration. The standard coatings are not optimized for this application in that they absorb too much solar energy to reach cryogenic temperatures and are designed to emit IR energy while at 300 K and not at cryogenic temperatures.

We have theoretically modeled a new selective coating designed to operate at cryogenic temperatures meeting NASA's new spacecraft needs. While the best existing selective surfaces absorb about 7% of the Sun's energy [4], these new coatings are predicted to absorb less than 0.1% of the Sun's energy. Consequently, surfaces coated with these new coatings can reach much lower temperatures than achievable through the use of existing materials.

The new coatings are based on the same concept as white paint. White paint is composed of very small scattering particles in a binder, both of which have very low absorption of visible radiation. So when visible radiation interacts with white paint, a large fraction is scattered backward, making the paint appear to be bright white. Very little energy makes it through the paint or is absorbed by it. Standard white paint, though, is not white over regions of the solar spectrum, since it absorbs portions of nonvisible radiation, such as ultraviolet (UV) and IR bands. Even off-the-shelf "white" thermal control coatings meant for use in space have significant absorption in these nonvisible bands. However, if the scatterers in the paint were composed of a material that was transparent, i.e. nonabsorbing, to most of the solar spectrum, and if the binder were composed of either vacuum or a different solar-band-transparent material, then this coating would appear to be white across nearly the entire solar spectrum, i.e. "Solar White."

This document presents details on the modeling of such Solar White coatings and predicts their performance as a function of material, coating thickness, and geometry (coating a flat plate, a cylinder, and a sphere). In addition, since the scattering of small particles is wavelength-dependent, and since the solar spectrum is extremely wide, we model the behavior of these coatings on a silver backing, enhancing their performance in far infrared.

1.1 Background

Selective surfaces are surfaces that have a designed emissivity that varies with wavelength. Many selective surfaces have been developed for use on Earth to absorb visible energy, e.g. high emissivity in the visible portion of the spectrum, but not absorb in the infrared, i.e. low emissivity in the infrared [1]. These surfaces become hot in the presence of sunlight and are used, for example, to improve the performance of solar furnaces. Other selective surfaces have been developed to reject the visible portion of the Sun's spectrum and to emit strongly in the infrared. These surfaces get cold in the presence of sunlight and have been heavily researched for use on Earth in developing, for example, roof coatings [5, 6]. But on Earth these coatings have limited performance due to atmospheric limitations on IR emission, atmospheric conduction and convection, and condensation [1].

However, the limitations in performance of selective surfaces on Earth are mostly eliminated in the vacuum of space. In space, thermal management is primarily a radiative, not conductive or convective issue, so the use of selective coatings (also known as thermal control coatings) is important. Selective surfaces have been space-tested [3] and used on both the Space Shuttle Orbiter and the Hubble Telescope (see Figure 1). In both cases, the selective surface was composed of a transparent plastic with an aluminized or silvered backing. This allows visible light to pass through the plastic, reflect off of the metal coating, and then pass back through the plastic, rejecting the visible light. But in the infrared, the plastic becomes opaque, acquiring a high emissivity and emitting substantial IR

radiation. So the primary use of this "second-surface mirror" type material is to provide net cooling for these spacecraft while in the presence of solar irradiance.

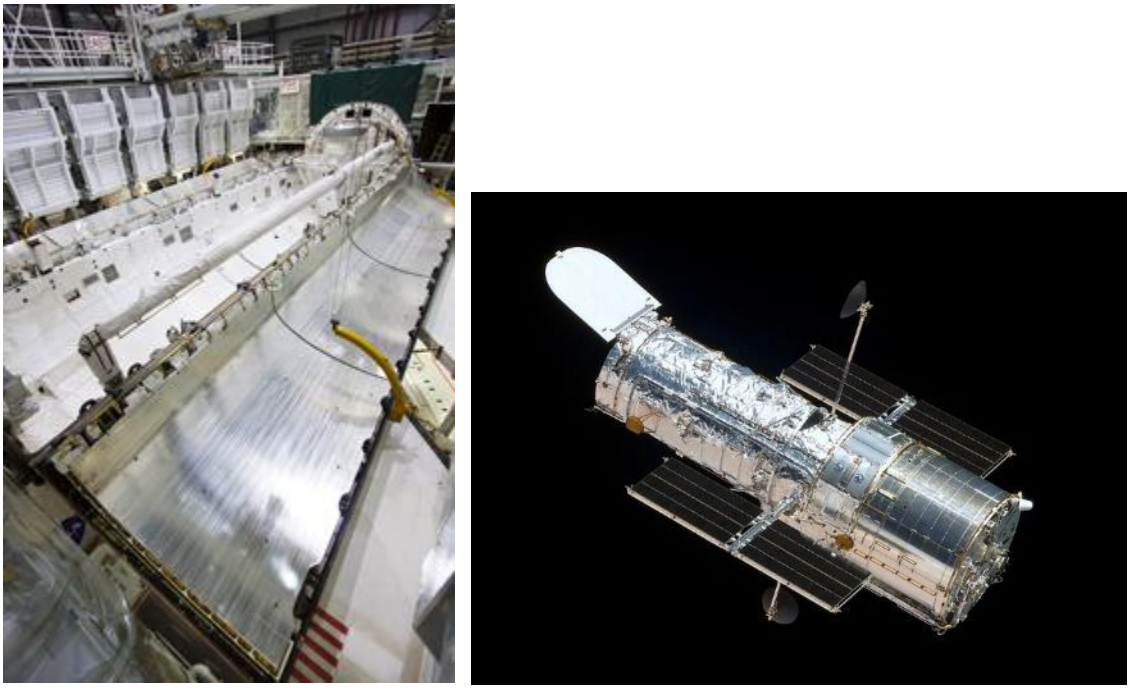

Figure 1. Examples of selective surfaces. The left picture shows the selective surface used on the Orbiter payload bay doors to help control the temperature of the vehicle in space. The right picture shows the selective surface used on the Hubble Telescope.

Within the literature there is a relatively simplistic model that can estimate the performance of a selective surface [2], which will be overviewed here to provide insight into the performance of these surfaces, but also to highlight the shortcomings of the standard coatings [2, 4]. We start with a simple formula that relates the energy absorbed to the energy emitted by an object located in space about 1 AU from the Sun:

$$A_S I \alpha = A \sigma \varepsilon T^4 ,$$

where A_S is the area perpendicular to the Sun, I is the total solar irradiance in watts per meter squared, α is an effective solar absorptance, A is the total emitting area of the object, σ is the Stefan Boltzmann constant (5.67×10^{-8} W/(m^{2}K^4)), ε is an effective emittance, and T is the temperature in kelvin. Solving for the temperature yields

$$T = \left[\frac{A_S}{A} \frac{I}{\sigma} \frac{\alpha}{\varepsilon} \right]^{1/4} .$$

For example, consider a small area on the Moon directly facing the Sun and assume the Moon is a graybody, i.e. a surface where the emissivity is not wavelength-dependent so that $\alpha = \varepsilon$. Also, the absorbing area and the emitting area are the same, so $A_S = A$. Estimating the total solar irradiance to be 1366 W/m^2, the temperature is predicted to be 394 K, which is 121 °C. This is very close to the maximum temperature seen on the Moon, 123 °C. We could also consider the case of the Earth, which is a rotating sphere, and ask what the average temperature should be for the Earth. In this case we again assume a graybody, but now the emitting area of a sphere is four times that of the

area perpendicular to the Sun, so $A_S = A/4$. Calculating the temperature yields 279 K, or 6 °C. The Earth's average temperature is about 14.6 °C. The difference is probably due to greenhouse effects and internal heat sources within the Earth.

So this simplistic model provides some insight into the role of geometry in the determination of the temperature of an object at 1 AU from the Sun. But now consider the role of the absorption and emission factors. α corresponds to the proportional amount of solar irradiance absorbed by the object while ε is the fractional ability to emit in the long-wave infrared. For the case of the Earth/sphere just described, where the sphere is at 279 K, the power balance absorption/emission curve is shown in Figure 2. The peak on the left is the solar irradiance, and the broad shallow curve, peaked at 10 µm, is the IR emission. Note that these two curves are well separated in wavelength and that separation is what allows selective surfaces to be realized.

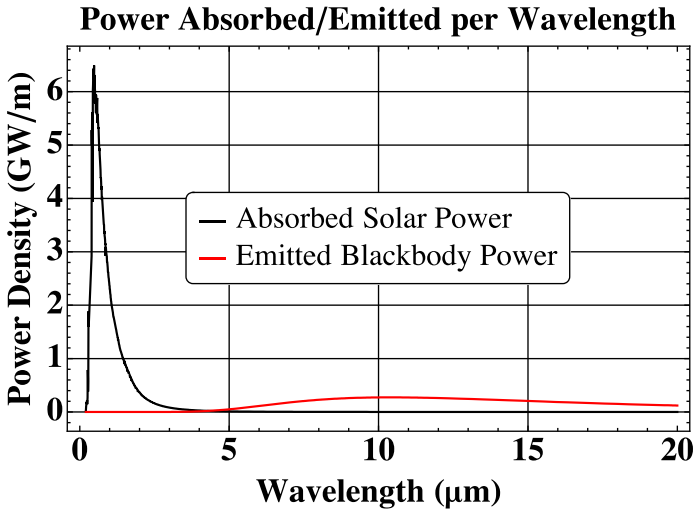

Figure 2. The power balance of a 1 m-radius sphere at 279 K. The black line shows the power absorbed by the object due to the Sun, and the red line is the power emitted as thermal radiation.

Considering only selective surfaces (also known as thermal control coatings) designed to cool a surface, the goal would be to develop a surface that reflects the solar energy in the visible portion of the spectrum, but emits in the infrared. Two different approaches have been developed to achieve this. The first one was mentioned above and is referred to as a second-surface mirror approach. In this case, a material is found that is transparent to the visible radiation but is black in the infrared and is coated on its backside with a broad-spectrum, typically metallic, reflector. Using this, sunlight will reflect off of the metal while IR radiation is emitted by the coating material. The second approach is to develop a white paint that is white, i.e. highly reflecting to solar radiation, yet is black in the infrared.

As mentioned above, clear plastic with a metal backing has been commonly used in space. Most of these have been some type of plastic with aluminum and have shown long-term degradation [3], but they have reasonable performance. Typical high-end values for these plastic second-surface mirrors are α = 0.07 and ε = 0.8, for a ratio of $\alpha / \varepsilon =$ 0.09 [3]. Henninger [2] states a best result of silver on 5 mil Teflon as α = 0.08 and ε = 0.8, for a ratio of 0.1. So coating a sphere with this material yields a temperature of about 153 K to 157 K, which is impressive since this is about −120 °C, but it is not sufficient to store LOX or operate superconductors.

The best white coatings are barium sulfate with polyvinyl alcohol: α = 0.06 and ε = 0.88 [2]; and AZW/LA-II by AZ Technology: α = 0.07 and ε = 0.91 [4]. The ratio for these is a bit better, 0.07 and 0.08, so the temperature of the sphere painted with the barium sulfate material would be 142 K—a bit better, but not there yet.

The problem with both of these approaches is that the materials being used are not rejecting enough of the Sun's energy. Silver absorbs substantial UV radiation and the white paints absorb some UV and some IR radiation. Better materials, as well as a better approach, are needed, and describing these and modeling performance will be the goal of the following sections.

1.2 Solar Spectrum

In order to model the performance of a coating in the presence of the Sun's irradiance, we need an accurate model of the solar spectral irradiance in deep space at 1 AU. We have decided to use the 2000 ASTM Standard Extraterrestrial Spectrum Reference E-490-00 for our solar irradiance calculations. This model provides irradiance data from 0.1195 μm in the deep ultraviolet to 1000 μm in the far infrared. Other than a small spike in the deep ultraviolet and some minor structural variations, the Sun's irradiance, shown in Figure 3, is similar to that of a 5778 K blackbody. The total area under this curve is 1366 W/m^2, i.e. the total irradiance of the Sun at 1 AU.

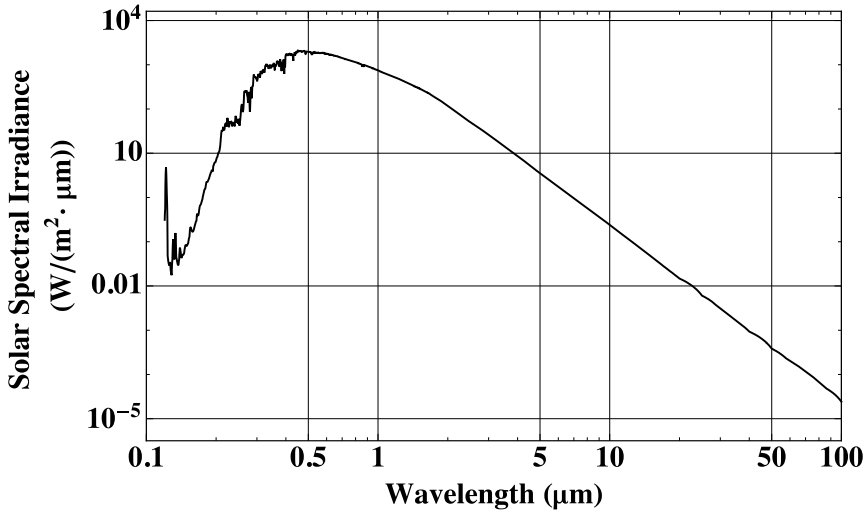

Figure 3. A standard spectrum for the Sun above the atmosphere from 0.1195 μm to 70 μm.

Since the goal is to reject as much of the Sun's energy as possible, it is important to consider the distribution of energy in this spectrum. So we start by considering the normalized integral of the solar spectrum shown in Figure 4.

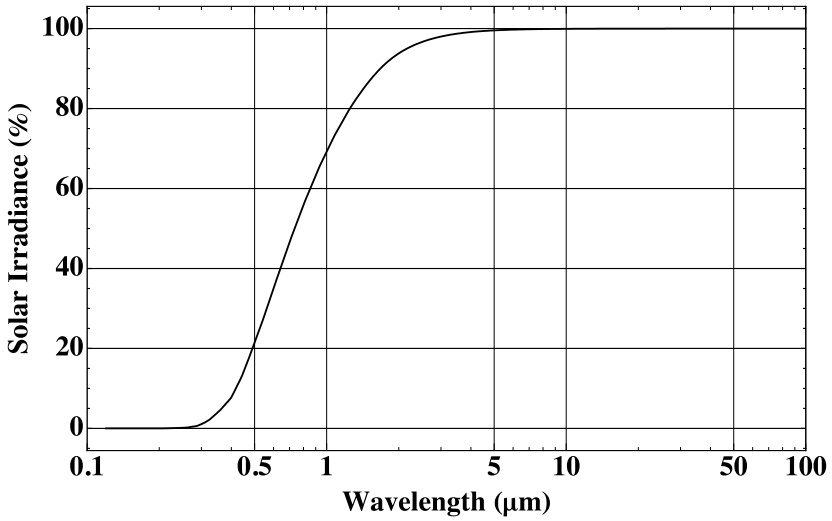

Figure 4. The integrated percentage of solar irradiance versus wavelength.

Figure 4 shows that most of the Sun's energy is located in a region between about 0.2 μm and 5 to 8 μm, but for our purposes, we would like better resolution. We started by expanding the UV region as shown in Figure 5. Note that at 0.3 μm we've already accumulated about 1% of the total irradiance, but that below 0.2 μm the contribution is negligible. In all of our calculations we will begin our calculations at 0.2 μm or shorter if material data is available.

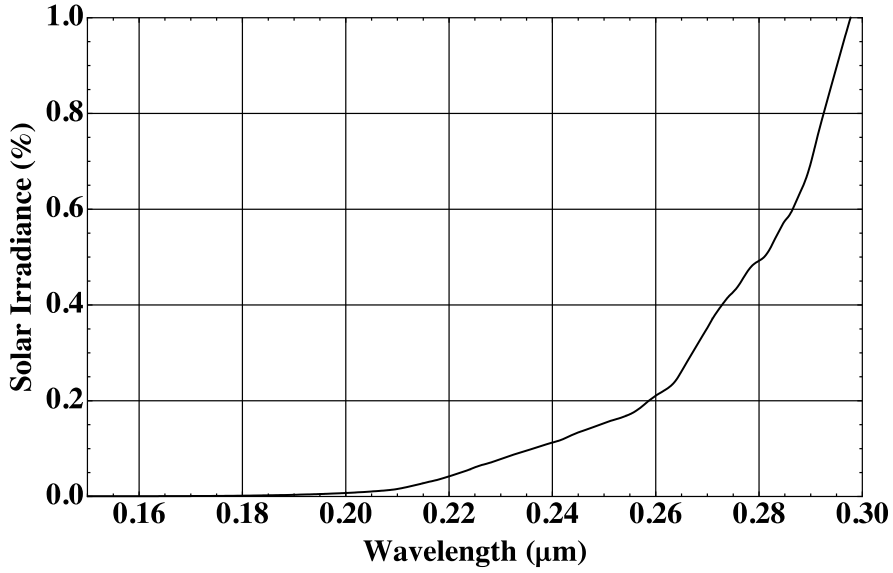

Figure 5. The integrated percentage of solar irradiance versus wavelength in the UV region.

Figure 6 shows the IR region expanded so that approximately the last 1% of the Sun's irradiance can be examined. Note that the curve is more gradual than in the ultraviolet, making the choice of a cutoff wavelength difficult. But we can see that having materials with transitions in this spectral region will lead to less than 1% of the Sun's energy being absorbed.

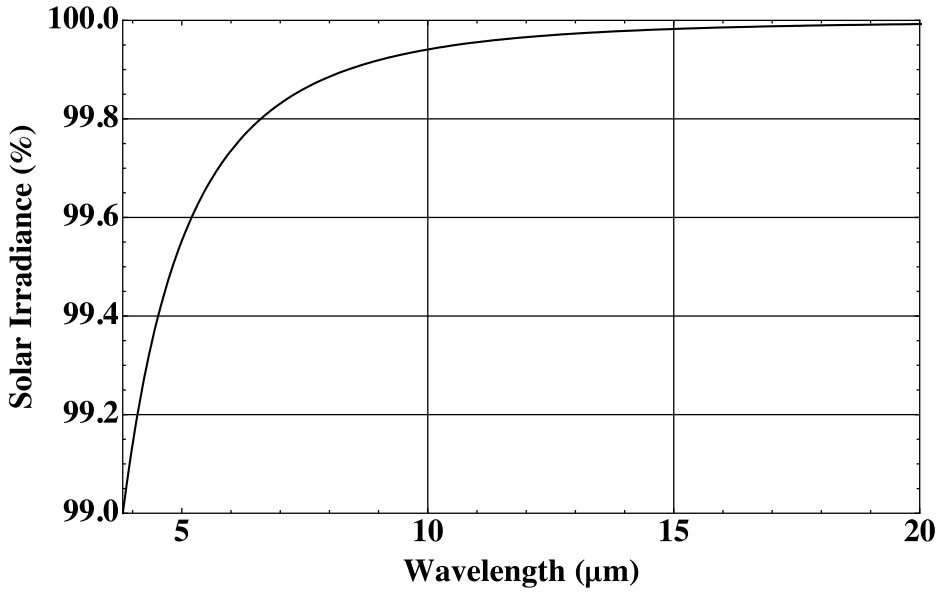

Figure 6. The integrated percentage of solar irradiance versus wavelength in the IR region.

In 1961 Hibbard stated that cryogenic temperatures could be reached if an ideal selective surface could be fabricated, i.e. one that was perfectly reflecting below a cutoff wavelength and perfectly emitting above this wavelength [7]. With the structure developed to this point, a quick check of this can be performed. First, assume that a perfect coating was developed with a cutoff at about 4 μm, so that only 1% of the Sun's energy was absorbed, i.e. a ratio $\alpha / \varepsilon =$ 0.01. For a sphere the temperature now drops to 88 K, below the 90 K needed to maintain LOX, but still too high to run a superconductor. But if we can find a material with a transition wavelength at about 8 μm, where only 0.1% of the Sun's energy is absorbed, then the sphere temperature will drop to about 50 K. This would not only allow superconductors to operate, but would allow LOX storage to occur at higher density and at lower pressure. Figure 7 shows the temperatures that could be achieved if a perfect material were available to coat a sphere at 1 AU from the Sun.

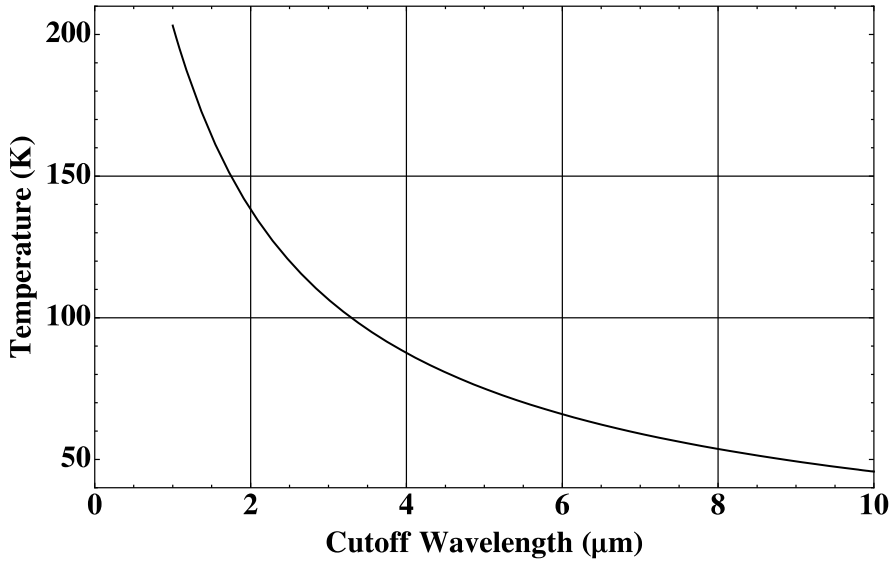

Figure 7. The equilibrium temperature of a sphere located 1 AU from the Sun if coated with an ideal material that was perfectly reflecting below a cutoff wavelength and perfectly absorbing/emitting above this cutoff wavelength.

1.3 Materials

In the selection of a material to face the solar radiation, whether for the first material of a second-surface mirror or for the diffusing material in a Solar White paint approach, it's important that as much of the solar energy be rejected as possible. For both applications this means that the material must be transmissive to as much of the Sun's spectrum as possible. As was shown in the previous section, an ideal material would be perfectly transparent from 0.2 µm to about 8 µm in order to achieve 50 K temperatures, but even if it is only transparent from 0.22 µm to 6 µm, it could be used.

In addition, it is important that this material have a high absorption, i.e. high emissivity, in the far infrared. The goal is to reach cryogenic temperatures, where the peak blackbody emission is around 40 µm. More specifically, from Wein's law, $\lambda_{MAX} = 0.0029 \text{ mK} / T$. So at 300 K, an object's peak emission is at 9.7 µm, at 90 K (LOX temperatures) the peak is at 32 µm, and at 77 K (LN_2 temperatures) the peak is at 40.3 µm. Since the goal is to achieve cryogenic temperatures, an ideal material would have a broad absorption/emission peak in the 30 µm to 70 µm range.

Fortunately, there are several optical materials with very broad passbands starting in the ultraviolet and extending into the far infrared. This is encouraging because even if a material meets the optical criteria it may not meet fabrication requirements that have not yet been determined. So having choices is important at this stage of the project.

In this section, most of the data has been obtained from the *Handbook of Optical Constants* [8] and from Crystran, a company that supplies optical windows and has an on-line database of optical materials [9]. Material data is often presented in one of two forms. The first, which is the more common in the literature, is to provide the real and complex indices of refraction for a material as a function of wavelength. We use both of these indices in our models, but the imaginary index of refraction provides loss data and is the one of most concern to us. As an example, the imaginary indices of refraction for magnesium fluoride (MgF_2) are shown in Figure 8.

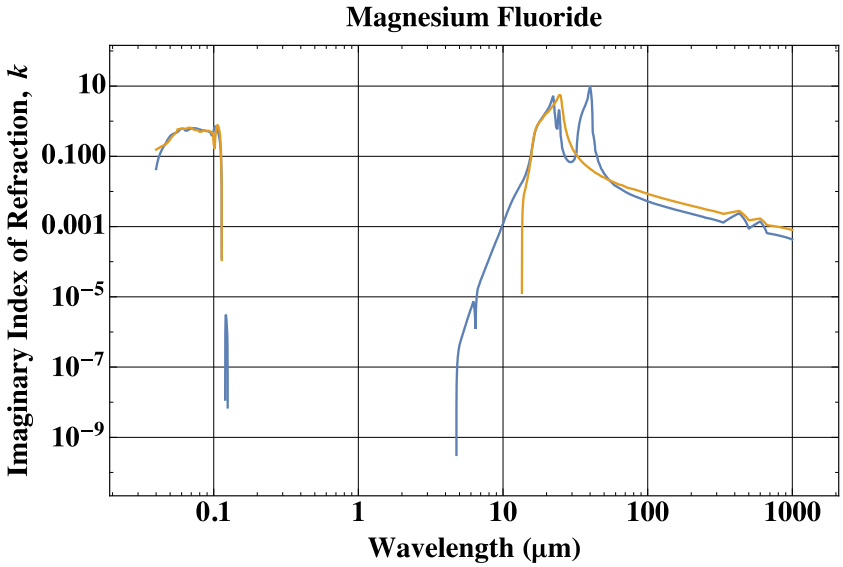

Figure 8. The imaginary indices of refraction for MgF_2 (ordinary is blue and extraordinary is tan).

There are two sets of data in this curve: the blue represents the ordinary ray and the tan the extraordinary ray in this birefringent crystal. Since the ordinary ray dominates and since, in our application, the orientation of the crystal is most likely random, we chose to always use the ordinary ray data in all calculations. This will introduce a small error in the analysis, but in many cases it is a slightly conservative error.

In the region of the passband, i.e. the region where the material is transparent, the losses are often so small that there are no measured values in the literature. Since we are only concerned with centimeter thickness of material (at most), we chose to simply set the imaginary index of refraction to zero in these regions.

In our modeling, we have decided to limit the thermal radiation of the materials listed below to wavelengths less than 100 μm because the emissivity at longer wavelengths can be temperature-sensitive, with the materials becoming less emissive as they cool down. So rather than use room-temperature data and obtain temperatures that are possibly too low, we chose to set the emissivity beyond 100 μm to zero, ensuring a degree of conservativeness in this aspect of the analysis.

It should also be mentioned that the imaginary index of refraction is often a measurement of loss in the material and not necessarily absorption. For example, Rayleigh scattering is a significant loss phenomenon in many materials, especially in the UV range, yet this energy is not absorbed. It is scattered away. For the present application, we are only concerned with absorbed energy, yet the literature sometimes does not separate absorbed energy from scattered energy, treating them both as losses and merging them into a common k value. In much of the following discussion, the handbook values [8] and vendor data, such as that from Crystran [9], disagree on the UV transmission of some materials, and we believe part of this is based on confusion between loss and scattering.

The imaginary index of refraction, k, is related to the transmission through a thickness, d, of material by the expression

$$T = \exp[-4\pi k[\lambda](d / \lambda)] .$$

(Note that if k only accounts for absorbed loss, then this relationship ignores scattering.)

The second way to present the transmission of a material is to publish its percentage transmission through a window of a given thickness, removing the reflection losses at the two air-to-material interfaces (many vendors simply publish raw measured data leaving in this reflection loss). In order to compare the literature values for the imaginary index of refraction with published transmission curves from vendors, the function shown above is used. Figure 9 shows the transmission through a 1 mm-thick window of MgF_2 using the index of refraction data from the function above and the equation for transmission.

So MgF_2 has a passband that starts well below 0.2 μm and reaches out to about 5 to 7 μm. This is not ideal for our application, but MgF_2 is readily available and commonly used in optics. It is also used as a coating material for glass, so having it available as an option is important. This is one of the materials we have chosen to consider in our analysis.

A window of MgF_2, 25 mm in diameter and 3 mm thick, costs $240 from Edmund Optics. The *Handbook of Optical Constants* [8] implies that the UV cutoff for MgF_2 is about 0.12 μm (MgF_2 is often used as an UV window for UV spectroscopy), which is well below our required cutoff wavelength. Crystran [9] shows it becoming fully transparent by 180 nm. In the infrared, it is still transmitting 75% energy through a 1 mm window at 8.33 μm. MgF_2 is similar to calcium fluoride (CaF_2) but shifted slightly toward shorter wavelengths.

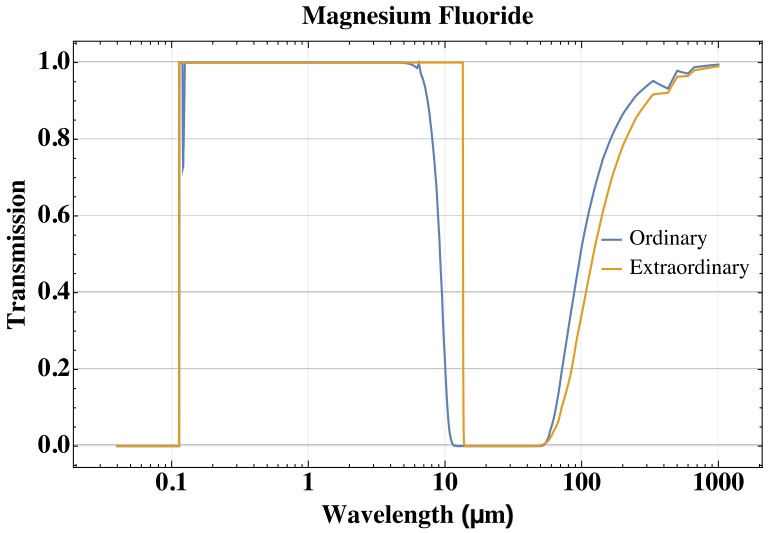

Figure 9. The transmission through 1 mm of MgF_2 for the two crystal orientations.

1.3.1 Calcium Fluoride (CaF_2)

CaF_2 is a readily available material for broadband optics and is not too expensive (a 25 mm-diameter, 3 mm-thick window costs $109 from Edmund Optics). The *Handbook of Optical Constants* [8] implies that the UV cutoff for CaF_2 is about 0.12 μm, which is well below our required cutoff wavelength. Crystran [9] shows a 5 mm window becoming partially transparent around 0.124 μm, but not becoming completely transparent until about 0.2 μm, which is good enough for our work (the difference may be due to Rayleigh scattering). In the infrared it is still transmitting 95% energy through a 1 mm window at 8.33 μm—see Figure 10. The only concern with CaF_2 is a limited emission region in the infrared. It may have difficulty radiating.

CaF_2 is a fairly good choice for early development due to its availability, cost, and relatively good transmission values. Figure 10 does not show the UV absorption for CaF_2, and birefringence data was not available.

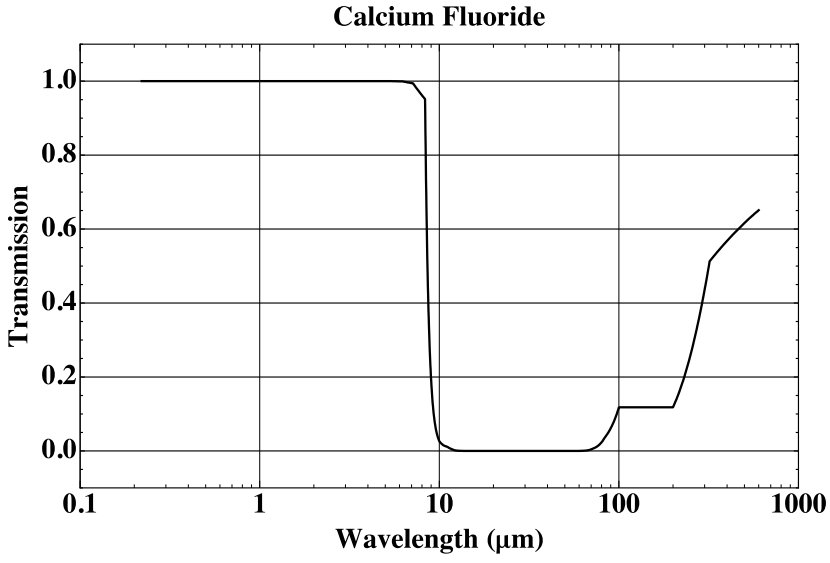

Figure 10. Transmission through 1 mm of CaF_2.

1.3.2 Barium Fluoride (BaF_2)

BaF_2 is another readily available material for broadband optics (a 25 mm-diameter, 3 mm-thick window costs $195 from Edmund Optics). The *Handbook of Optical Constants* [8] implies that the UV cutoff for BaF_2 is between 0.13 μm and 0.14 μm (the imaginary index drops eight orders of magnitude across this range), which is well below our required cutoff wavelength. Surprisingly, Crystran [9] shows it still absorbing some UV radiation out to 180 nm, but this is still OK for our use (again, this might be Rayleigh scattering). In the infrared it is still transmitting 99.9% energy through a 1 mm window at 8.5 μm. At 12 μm, it transmits 92% through a 1 mm window (at 13 μm, it transmits 82%, and 36% at 15.1 μm). BaF_2 can be used up to 800 °C and is the most resistant to high-energy radiation of any of the optical fluorides. BaF_2 has its peak emission in the 30 μm to 60 μm range, which is ideal for our purposes. Figure 11 and Figure 12 show the imaginary index of refraction and the transmission through a 1 mm window.

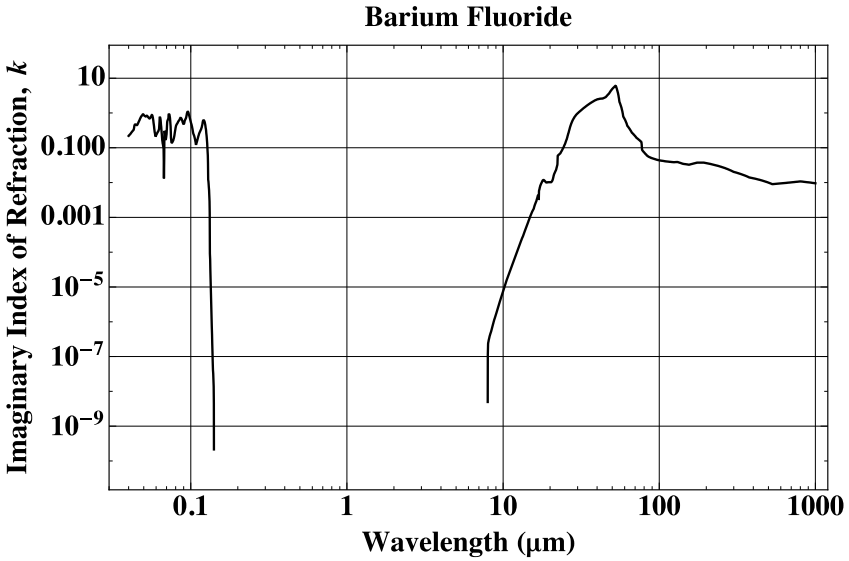

Figure 11. The imaginary index of refraction for BaF_2.

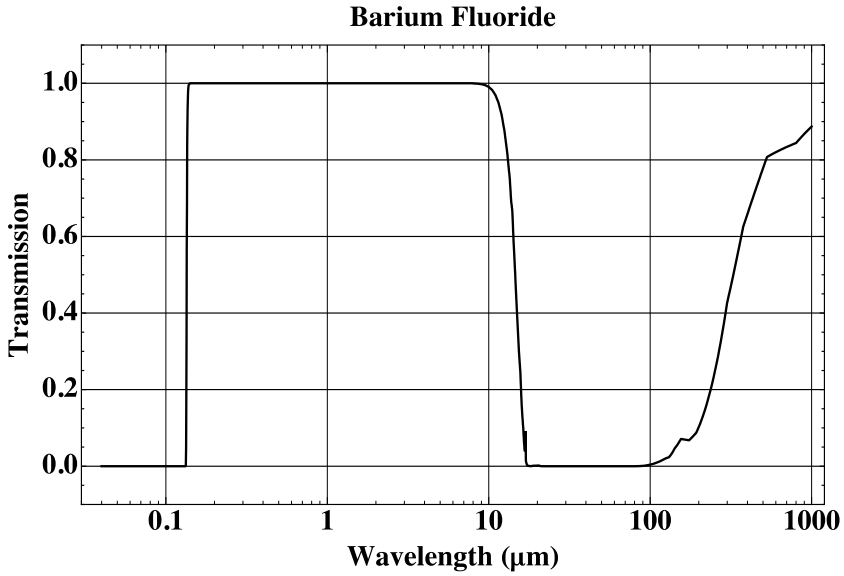

Figure 12. The transmission through 1 mm of BaF_2.

With BaF_2, as opposed to MgF_2, we give up a little UV range in a region we don't need and obtain a greater range into the far infrared. Note that the transmission is low out to 100 μm, a good feature for our requirements. Another benefit of this material is that it will not absorb much of the thermal energy emitted by 300 K blackbodies, though modeling is still needed to see how useful that will be. Overall, this may be the best material for our purposes, and we will use it in our models.

1.3.3 Sodium Chloride (NaCl)

NaCl is another readily available and inexpensive material for broadband optics (a 25 mm-diameter, 5 mm-thick window costs $52.50 from Edmund Optics). The *Handbook of Optical Constants* [8] implies that the UV cutoff for NaCl is between 0.163 μm and 0.173 μm (the imaginary index drops six orders of magnitude across this range [see Figure 13]). The transmission at 0.1743 μm through a 1 mm window is 97% (see Figure 14). It continues to drop as the wavelength increases, but the handbook [8] doesn't provide another data point until the wavelength is 0.35. If we use NaCl we'll need to find better UV transmission data. Crystran [9] shows it absorbing UV radiation out past 300 nm, so it may not be appropriate for solar rejection. But then again, this might just be Rayleigh scattering. One of the benefits of NaCl is its range of transparency in the far infrared. It transmits 94% of the 16.67 μm radiation that impinges on a 1 mm-thick window (86% at 18.18 μm, 68% at 20 μm)—ignoring the surface reflections.

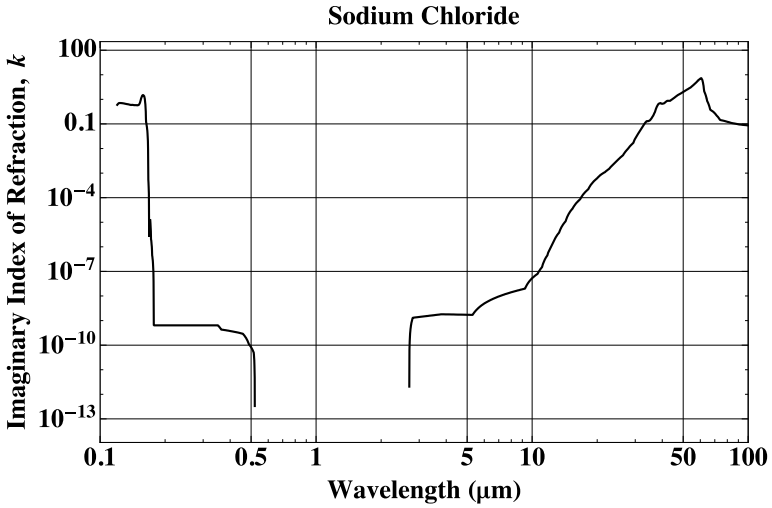

Figure 13. The imaginary index of NaCl.

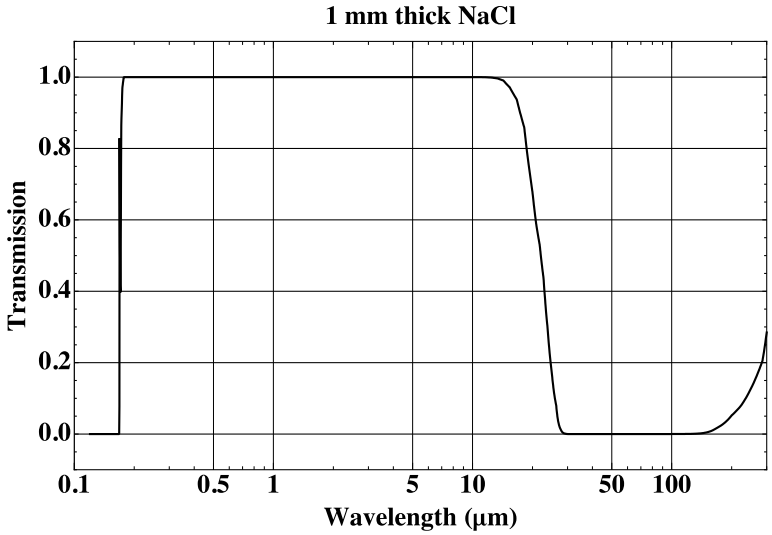

Figure 14. The transmission through 1 mm of NaCl.

NaCl might be a good choice for use as a Solar White material, though we need better UV data. It is possible that NaCl might be preferable to BaF_2. Also, it might be the ideal material for blocking 300 K radiation, as well as solar radiation. Even though some of the data shown above is uncertain, we have decided to use it, and thus include NaCl in our models.

1.3.4 Sapphire (Al_2O_3)

Sapphire is a very hard material that is readily available (a 25.4 mm-diameter, 2.25 mm-thick window costs $72.50 from Edmund Optics). It was our first choice for consideration because we felt that it had a sufficiently wide passband and that it might be acceptable as a spaceflight material. Figure 15 shows the imaginary portion of the index of refraction for the two crystal axes: the ordinary and the extraordinary.

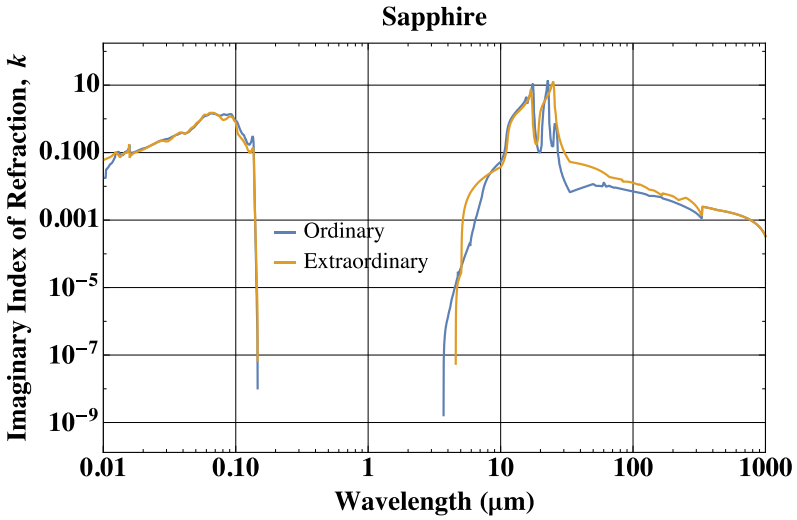

Figure 15. The imaginary index of sapphire.

The UV transition for sapphire occurs at about 0.145 µm, so it meets the UV criteria. (Crystan [9] shows that this is not strictly true and that even a UV-grade sapphire might absorb some radiation in the 200 nm to 250 nm range. Again, this might be due to Rayleigh scattering.) But in the infrared it begins to show absorbance at about 5.5 µm. At 5.556 µm, its imaginary index is 0.00012. As an example, if we use a 1 mm-thick layer of sapphire as our test thickness, we would transmit about 76% of this radiation. Crystran [9] states that a 1 mm sample should transmit 70%, which is in rough agreement.

Figure 16 shows the transmission through 1 mm of sapphire using the imaginary index of refraction data shown above. One of the weaknesses of sapphire that has arisen in our modeling is that thin films have relatively low emissivity in the critical 30 µm to 100 µm range. We used this material in our early models, but have decided not use it in our final models.

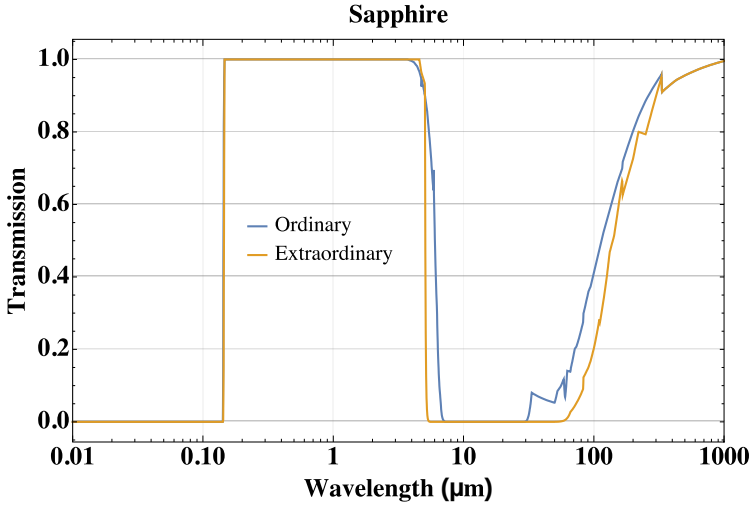

Figure 16. The transmission through 1 mm of sapphire.

There are many other optical materials available and rather than discuss each one separately, we have summarized their properties and those of the materials already presented in Table 1. In Section 1.10, we show modeling results for seven materials: MgF_2, BaF_2, CsBr, KCl, NaCl, KBr, and CaF_2.

Table 1. Possible Solar White materials, with comments.

Material	UV Transition (μm)	IR Transition (μm)	Comments
Sapphire	0.18	5.5	Relatively poor IR transmission, but could be used in higher-temperature applications if a higher-index material is needed.
CaF_2	0.12	8–9	Good available material, but some data seems to be missing from the literature.
MgF_2	0.12	8	Good, but slightly poorer than CaF_2 due to IR absorption and more expensive.
BaF_2	0.14	12–14	Very good. Rugged, available, wide UV-IR band. Good far-IR emission.
SrF_2	0.13 (full trans by 0.2)	10	Properties between CaF_2 and BaF_2. Not a common material.
NaCl	0.17–0.3	20	Needs UV check. Might be good to block 300 K. It is possible that this might be better than BaF_2, but data is lacking.
CsBr	0.20	30–40	A possible material. Due to its very wide passband, it might be appropriate for blocking 300 K radiation. Might have a small absorption at 260 nm that could hurt our application. http://www.crystran.co.uk/optical-materials/caesium-bromide-csbr
NaF	0.14 (full trans by 0.2)	10	Lowest index of any common optical material. Might be worth looking at, but far-IR emission doesn't look good.
LiF	0.11 (but full trans at 0.2)	6	Shortest UV transmission of any material. Doesn't go far enough into the infrared for our purposes.
KCl	0.18 (but soft-might be OK)	18	Might be worth looking at. Inexpensive. The far-IR emission might be OK.
KBr	0.21 (but soft)	20–30	Probably too much UV absorption.

1.4 Silver (Ag)

It is important to discuss the properties of silver as a reflector [10, 11, 12]. We use three references from the literature, providing the real and imaginary indices of refraction—see Figure 17—to model silver. Using the complex form of Fresnel's equations (provided in the subsequent sections), a net fractional power reflection can be calculated, which is shown in Figure 18.

Silver is the best metallic reflector of all solid metals, yet it has a serious problem in the ultraviolet starting at about 0.3 μm. For this and all shorter wavelengths silver absorbs most of the impinging energy, yet, as can be seen in Figure 18, the solar energy in this region is not insignificant. Also, silver has significant absorption through the visible. This is the primary reason that the plastic second-surface mirrors with silver or aluminum backings still absorb substantial amounts of solar radiation. We very carefully modeled a sphere, coated with silver and then coated with MgF_2, to see how this second-surface mirror approach would work and obtained a temperature of 153 K. This relatively high temperature is almost entirely due to the absorption of silver. So we need to drop second-surface mirrors from consideration and in our designs minimize the amount of UV light that interacts with silver, though note that the reflectivity is very high in the far infrared.

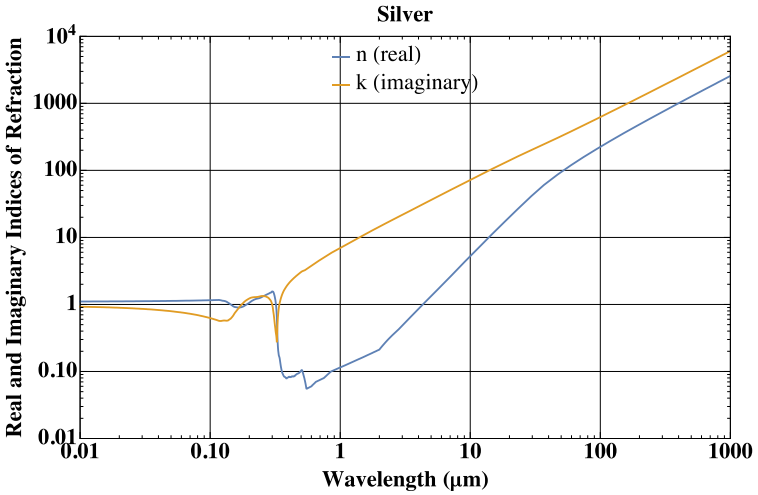

Figure 17. The real and imaginary indices of refraction for silver.

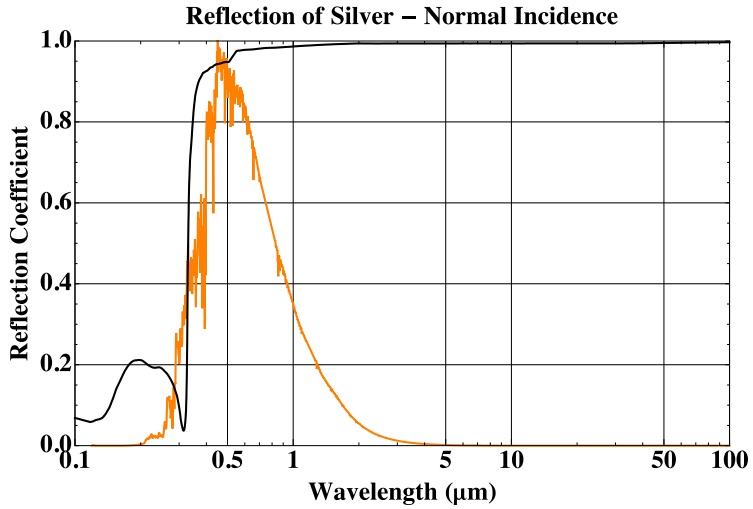

Figure 18. The normal incidence reflection coefficient of silver, with the solar spectrum superimposed for reference.

1.5 Radiation Transfer Theory

Summarizing the situation to this point, in order to achieve cryogenic equilibrium temperatures in deep space (1 AU from the Sun, far from the Earth), it is necessary to construct an object coated with a surface that can reject at least 99% of the Sun's energy while still emitting well as a blackbody in the far infrared. The first obvious choice, a second-surface mirror, fails due to UV absorption by most metals. Silver, being the best reflector of the solid metals, has an absorption around 300 nm, where the Sun's emission is still substantial. The next choice is dielectric mirrors, which have been demonstrated to reflect better than 99% of radiation from 300 to 1100 nm, but these likely fail as well. The Sun's energy must be rejected out to at least 5 μm, and many dielectric materials become absorbers at longer wavelengths. Even so, this approach might work, but as one vendor put it, a two-year, six-figure cost would probably not reach this goal, so it is not a likely near-term solution to the problem.

However, there is a third option, namely, constructing a diffuse scatterer from a material that is transparent to the solar spectrum. A powder, foam, or other construct composed of fine particles of a transparent material will appear white due to the scattering of light. Such a construct could reject substantial light, but the question is whether

it can reject enough to achieve cryogenic temperature in deep space. To partially answer this, imagine such a scattering material were composed of CaF_2, which is highly transparent over most of the solar spectrum, from the ultraviolet out to 7 to 8 μm. When sunlight hits such a material, there is essentially no absorption. The light instead scatters from the particles multiple times until it reaches a boundary from which it can escape. So if most of the light emerges from surfaces that face deep space, then the solar energy will not reach the underlying material where it can be absorbed, essentially rejecting the solar energy.

As an example in the visible-light region, consider the tile used on the Space Shuttle Orbiter. This tile is composed of nearly pure glass fibers in a rigid random matrix. Glass has essentially no absorption in the visible, so when a flashlight is used to illuminate a small cube of this material, it lights up as a bright white surface as shown in Figure 19. In the left picture, the light saturates the camera. In the right picture, the light that makes it through the cube is shown. This picture was taken with the room lights off, allowing the camera to image the small amount of light that does progress through the cube.

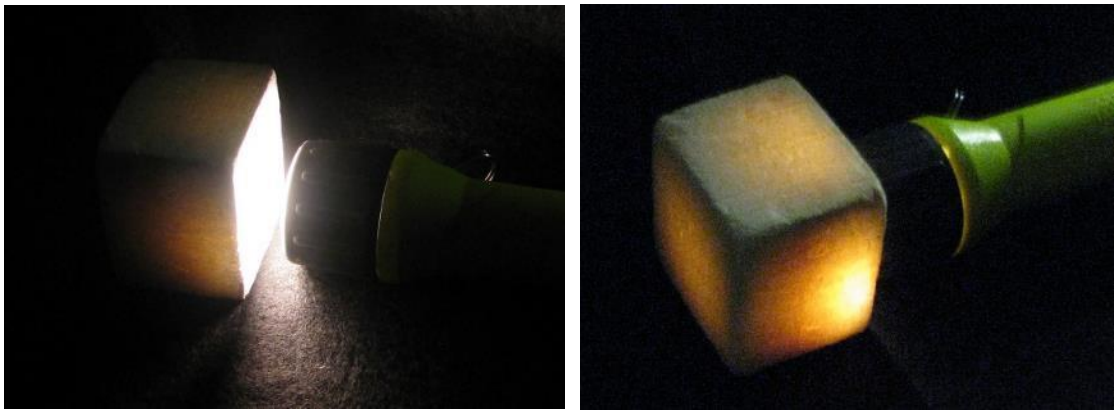

Figure 19. Scattering and transference of light. A flashlight is used to show how much light scatters back from a 2-inch cube of Space Shuttle Orbiter tile material and how much light makes it through. Nearly all of the light scatters backward.

Developing a model of the performance of these materials requires expressions developed in the field of radiation transfer. S. Chandrasekhar's book *Radiative Transfer* [13] develops the theory of this field, but for our case, a simpler development, presented in "Radiation through a Foggy Atmosphere," by Arthur Schuster [14], was adapted for our modeling.

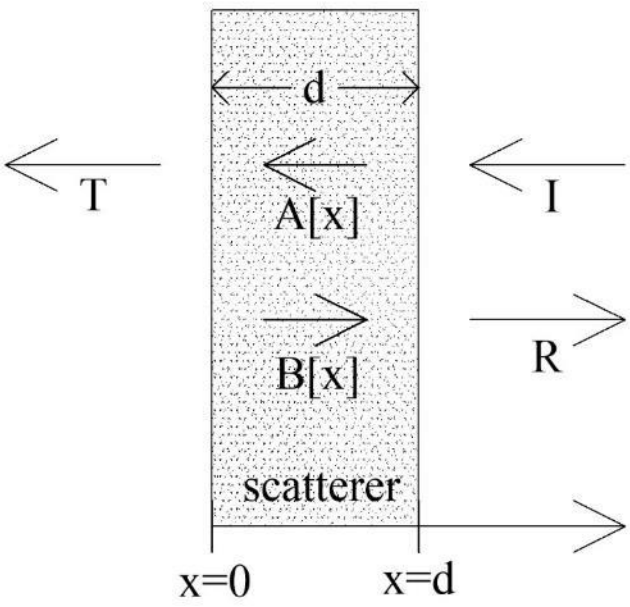

Figure 20. A sheet of scattering material with light impinging on it from the right.

Let's start with a sheet composed of an isotropic homogeneous scattering material as shown in Figure 20 (above). This is a diffuse scatterer of thickness, d, with incident radiant intensity coming in from the right, I, the transmitted intensity, T, leaving to the left, and the reflected radiation, R, leaving to the right. Within the material there is a backward-propagating intensity field, $A[x]$, and a forward-propagating intensity field, $B[x]$. We will assume a scattering coefficient, s, and an absorption coefficient, κ. The differential equations describing the propagation of optical intensity are given by

$$\begin{aligned} \frac{dA[x]}{dx} &= \kappa A[x] + \frac{1}{2} s(A[x] - B[x]) \\ \frac{dB[x]}{dx} &= -\kappa B[x] + \frac{1}{2} s(A[x] - B[x]) \end{aligned} . \tag{1}$$

From this we see that

$$\begin{aligned} \frac{d(A[x] - B[x])}{dx} &= \kappa(A[x] + B[x]) \\ \frac{d(A[x] + B[x])}{dx} &= (\kappa + s)(A[x] - B[x]) \end{aligned} , \tag{2}$$

indicating that $A[x] - B[x] = F[x]$, the flux, is not a constant. If we let the energy density, $U[x]$, be defined as $U[x] = A[x] + B[x]$, then the differential equations become

$$\frac{d\,F[x]}{dx} = \kappa U[x] \qquad \frac{d\,U[x]}{dx} = (\kappa + s)F[x] .$$

Taking the second derivative of each of these and simplifying yields

$$\frac{d^2F[x]}{dx^2} = \kappa(\kappa+s)F[x] \qquad \frac{d^2U[x]}{dx^2} = \kappa(\kappa+s)U[x]\,.$$

Consider the energy density equation first. It has the solution

$$U[x] = A[x] + B[x] = c_1 \exp[\alpha(\kappa+s)x] + c_2 \exp[-\alpha(\kappa+s)x]\,, \tag{3}$$

where $\alpha = \sqrt{\kappa/(\kappa+s)}$. Taking the derivative of this yields

$$\frac{dU[x]}{dx} = c_1\alpha(\kappa+s)\exp[\alpha(\kappa+s)x] - c_2\alpha(\kappa+s)\exp[-\alpha(\kappa+s)x]\,,$$

from which $F[x]$ can be found:

$$F[x] = A[x] - B[x] = \frac{dU[x]}{dx}/(\kappa+s) = c_1\alpha\exp[\alpha(\kappa+s)x] - c_2\alpha\exp[-\alpha(\kappa+s)x]\,. \tag{4}$$

Combining Equations 3 and 4 yields expressions for $A[x]$ and $B[x]$:

$$\begin{aligned} 2A[x] &= c_1(1+\alpha)\exp[\alpha(\kappa+s)x] + c_2(1-\alpha)\exp[-\alpha(\kappa+s)x] \\ 2B[x] &= c_1(1-\alpha)\exp[\alpha(\kappa+s)x] + c_2(1+\alpha)\exp[-\alpha(\kappa+s)x] \end{aligned}. \tag{5}$$

Now insert the boundary conditions, where the goal is to find the transmission and reflection coefficients knowing that the incoming intensity arrives from the right and that no energy is arriving from the left. So

$$\begin{aligned} A[0] &= T \\ A[d] &= I \\ B[0] &= 0 \\ B[d] &= R \end{aligned}.$$

Using $B[0] = 0$ and $A[d] = I$ in Equation 5 yields

$$\begin{aligned} 2A[d] = 2I &= c_1(1+\alpha)\exp[\alpha(\kappa+s)d] + c_2(1-\alpha)\exp[-\alpha(\kappa+s)d] \\ 2B[0] = 0 &= c_1(1-\alpha) + c_2(1+\alpha) \end{aligned}.$$

Using these, the coefficients c_1 and c_2 can be found, and full expressions for $A[x]$ and $B[x]$ can be written as

$$\begin{aligned} A[x] &= I\,\frac{(2\kappa+s)\sinh[\sqrt{\kappa(\kappa+s)}x] + 2\sqrt{\kappa(\kappa+s)}\cosh[\sqrt{\kappa(\kappa+s)}x]}{(2\kappa+s)\sinh[\sqrt{\kappa(\kappa+s)}d] + 2\sqrt{\kappa(\kappa+s)}\cosh[\sqrt{\kappa(\kappa+s)}d]} \\ B[x] &= I\,\frac{s\sinh[\sqrt{\kappa(\kappa+s)}x]}{(2\kappa+s)\sinh[\sqrt{\kappa(\kappa+s)}d] + 2\sqrt{\kappa(\kappa+s)}\cosh[\sqrt{\kappa(\kappa+s)}d]} \end{aligned}.$$

An example is shown in Figure 21, where s = 0.33 μm^{-1}, the thickness of the layer is 1 mm, the absorption is 0.00004 μm^{-1}, and the initial intensity is 1. Even with such a low loss, the decay is enhanced since it is governed by $\sqrt{\kappa(\kappa+s)}$ = 0.0036.

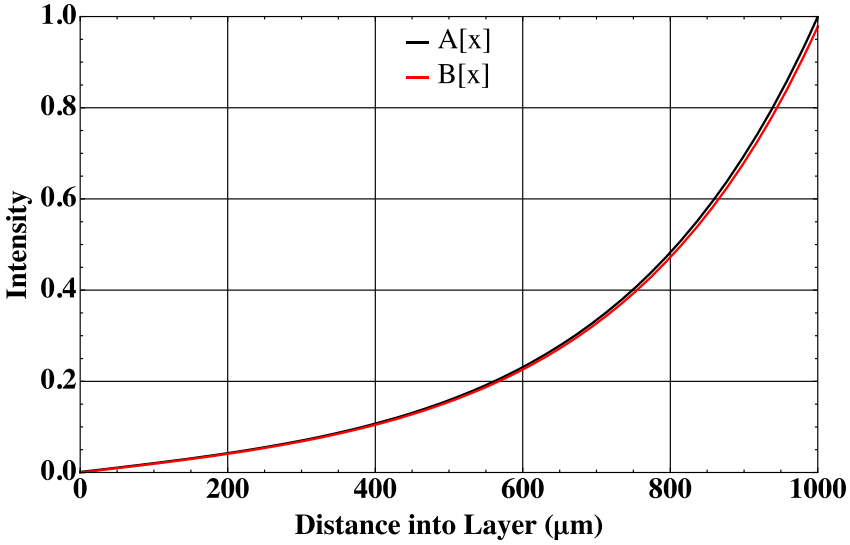

Figure 21. A transmission example, described in the text, in which the transmission through the material is only 0.0011, and the reflection is 97.82%. About 2% of the energy is absorbed into the scattering layer.

One way to help improve the performance of the coating is to add a silver backing to the scatterer. In the ultraviolet, where the scatterer works well, the silver will see very little light; but in the mid infrared, where the scatterer allows more light through, the silver will act as a very low loss reflector, complementing the diffuse scatterer. Figure 22 shows the situation.

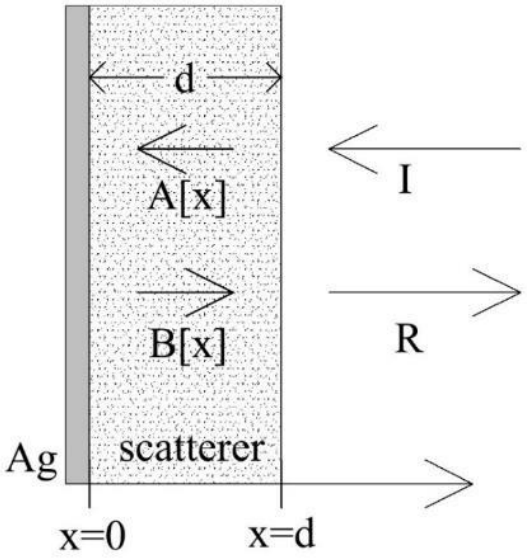

Figure 22. A sheet of scattering material with a silver backing, with light impinging on it from the right.

This configuration can be solved using the same differential equations, shown in Equation 1, but with different boundary conditions. The new boundary conditions are

$$A[d] = I$$
$$B[0] = r_{Ag} A[0],$$
$$B[d] = R$$

where r_{Ag} is the reflectivity of the silver.

Now we can solve Equation 1 to obtain the reflection from the scatterer with a silver backing, directly yielding

$$B[d] = R = I \frac{2r_{Ag}\sqrt{\kappa(\kappa+s)}\cosh[d\sqrt{\kappa(\kappa+s)}] + (s - r_{Ag}(2\kappa+s))\sinh[d\sqrt{\kappa(\kappa+s)}]}{2\sqrt{\kappa(\kappa+s)}\cosh[d\sqrt{\kappa(\kappa+s)}] + (2\kappa+s-r_{Ag}s)\sinh[d\sqrt{\kappa(\kappa+s)}]}. \quad (6)$$

Equation 6 is the key result of the analysis and provides a closed-form expression for the light that backscatters from a diffuse material with a silver backing as a function the material parameters and the reflectivity of the silver. However, we have problems. The value for the absorption coefficient, κ, is unknown; we have no insight as to how this relates to the complex index of refraction for a given material. In addition, we do not have a model predicting values for the scattering coefficient, s, and we need to determine the reflectivity for silver with scattered light impinging on it. Section 1.6 will address these questions.

Before moving on, it will be useful to find an expression for R/I when the absorption is zero. Taking the limit of Equation 6 as κ goes to zero yields

$$B[d] = \frac{ds + r_{Ag}(2-ds)}{2 + ds - r_{Ag}ds}. \quad (7)$$

If the reflectivity of the silver approaches 1, then $B[d] = r_{Ag}$, as expected.

1.6 Scattering Theory

An alternate way to model optical scattering is to ignore the forward and backward waves and just model the total optical flux as being completely scattered within a discrete spatial volume. This model is simpler than the 1-D differential case above, but has some discretization problems. Yet it allows extension to 3-D and provides additional, necessary, physical insight.

Consider Figure 23, showing a series of scattering cubes of side length, l. We assume that the light entering each cube is isotropically scattered. This light then leaves the cube equally through each of the six surfaces. We assume incoming light from the left, and we adopt periodic boundary conditions so that when light leaves the top of a cube, it reenters the same cube from the bottom and similarly on all four outer sides. So if we number the cubes, $j \in (1, N)$, then for internal cubes, at steady state,

$$I[j] = 1/6(I[j-1] + I[j+1]) + (2/3)I[j].$$

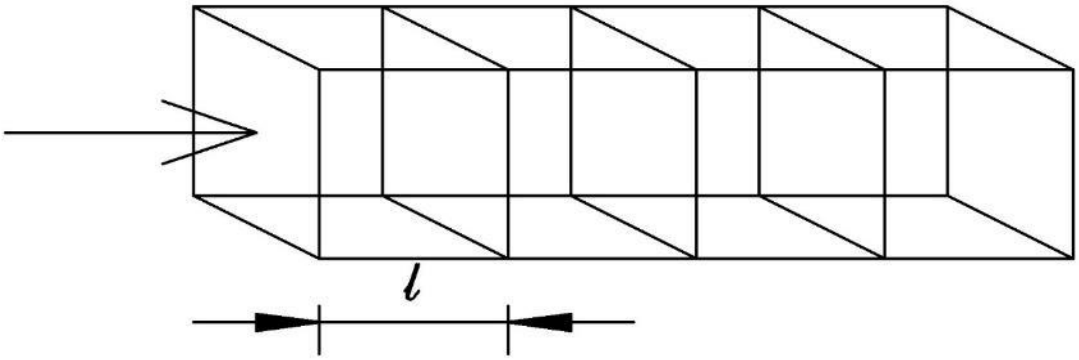

Figure 23. A series of scattering cubes.

Solving this set of simultaneous equations then leads to solutions nearly identical (to within the discretization) to those obtained using the lossless differential equations described earlier. However, there is one significant difference. The radiation theory equations state that the flux within the first cube is two times that of the incoming radiation, and the discrete scattering model states that the total flux in the first cube is six times the incoming radiation. The reason for the difference is that the 1-D differential equation case ignores sideways scattering, which is clearly incorrect. Scattering occurs in all directions.

Loss can be added to the discrete model by stating that the light in a cube interacts once equally with the material within the cube. In other words, if unit power enters the cube, then after one scattering period, the amount of light leaving the cube is estimated to be

$$\exp[-\alpha l] = \exp[-4\pi k f l / \lambda],$$

where α is a material absorption coefficient that can be obtained from the imaginary index of refraction, k, the wavelength, λ, and the fill factor, f (ratio of volume of material to total volume). So now the steady-state equation becomes

$$I[j] = \exp[-\alpha l]\{1/6(I[j-1] + I[j+1]) + (2/3)I[j]\}.$$

Solving these equations yields functional forms very similar to those obtained from Equation 6.

The reason for developing this alternate model is that the differential equation model assumes an absorption coefficient, κ, and a scattering coefficient, s, but it isn't clear what values these should be set to. κ is not the material absorption coefficient, α, because the material parameter describes absorption by light passing through only one scattering cell. Matching the predictions of the two models allows the following associations to be obtained:

$$\kappa = 3\alpha \quad \text{and} \quad s = 2/l,$$

yielding

$$\kappa = 3(4\pi)kf / \lambda. \tag{8}$$

This result provides one of the missing pieces needed in the differential equation solution shown in Equation 6. Also, if we define N to be the number of scattering layers, i.e. $N = d / l$, then $ds = 2N$ and the form for the reflectivity of the Solar White coating when the absorption coefficient is zero becomes

$$B[d] = \frac{N + r_{Ag}(1-N)}{1 + N - Nr_{Ag}}. \tag{9}$$

We still need to determine a reasonable value for the scattering parameter, s, and to do that we'll need some results from Mie scattering and insight from paint concepts. It should be mentioned that small errors in determining s will not affect the overall performance of the coating; it only affects the total thickness needed to achieve a given level of performance. So we do not need to determine s exactly in order to theoretically verify the performance of the proposed cryogenic selective surface. To find a functional form for s we start by assuming that three interactions with lossless particles of size a causes short-wavelength light to be totally scattered, assuming that the particles are in vacuum or in air and have an index of 1.5. This assumption implies that $l = 3a / f^{1/3}$ or $s = 2f^{1/3} / (3a)$ in this limit. To account for changes in scattering with wavelength we performed a functional fit of a standard Mie scattering plot for a perfect sphere, but smoothed it to account for variations in particle size. We assumed a roughly three times enhancement in scattering when the wavelength roughly matches the circumference of the scatterers, using data supplied by the paint industry [15]. Finally, we added an index dependence based on standard Rayleigh scattering results [16]. Doing this yielded the following function for the scattering parameter as a function of wavelength:

$$s = \frac{2f^{1/3}}{3a}\frac{289}{25}\left|\frac{\tilde{n}^2 - 1}{\tilde{n}^2 + 2}\right|^2 \frac{1 + 3/(1 + (1 - 10a/(3\lambda))^2)}{1 + (3\lambda/(10a))^4},$$

where $\tilde{n}$ is the complex index of refraction. From the Dupont Titanium Dioxide Brochure [15], we found that paint particles are typically between 0.2 μm and 0.3 μm in diameter. This size is chosen in order to maximize the scattering of visible light. So, for our analysis we decided to use 0.25 μm as a particle diameter since the peak of the Sun's energy is in the visible band. From this same document we chose a fill factor, f, equal to 0.3. With these choices the scattering function can be plotted as shown in Figure 24.

As the wavelength gets long, the scattering length will eventually become so long that the coating will not scatter light. Instead, this long-wavelength light will see the very small particles as part of a continuous medium and there will be no scattering. For example, at 7 μm, the scattering function has dropped to about 0.001 μm^{-1}, indicating an isotropic scattering length of 2 mm. So if the coating is 2 mm thick, it will only scatter the light once and the benefit found from the use of a diffuse scattering surface will be minimal. When the silver is placed under the diffuse scatter, this limitation is removed.

The joint use of silver and a diffuse coating yields a wonderfully cooperative reflective surface. The diffuse coating operates extremely well for short wavelengths where the scattering is high, preventing the visible and UV radiation from reaching the silver, where it would be absorbed. But in the infrared, where the diffuse surface begins to scatter less effectively and where more radiation begins to get through the scattering layer, the silver is a very efficient reflector and takes over the task of rejecting the Sun's radiation.

In order to complete the analysis, we have to model the absorption, and hence find the emission, of this surface in the far-IR wavelengths beyond 10 μm. In this region, we need to treat the scattering layer as a continuous medium and need to develop an alternative optical model to predict the emissivity. We will develop this model in Section 1.7.

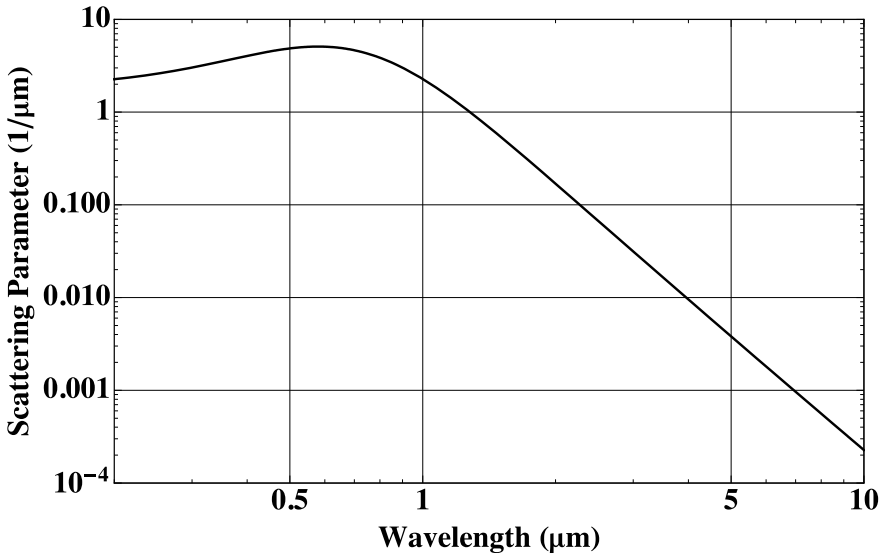

Figure 24. The scattering function used in the model.

However, before doing that, we need to find an expression for the reflectivity of silver, r_{Ag}, to be used in Equation 6. In order to model the reflectivity of silver, we assume that the rays of light in the scatterer are scattered in all directions equally, so the light hitting the silver is coming in isotropically. To calculate this, we start with the complex form of Snell's law, which connects the incoming angle, ν, to the transmission angle of the radiation into the silver, η,

$$\sin[\eta] = \sin[\nu] / (n_S[\lambda] + i\, k_S[\lambda]),$$

where $n_S[\lambda]$ and $k_S[\lambda]$ are the real and imaginary indices of refraction for silver. Once the complex angle η has been found, the Fresnel equations for the reflection from air or vacuum to silver can be used to find the amplitude reflection coefficients, $r_{SN}[\nu,\lambda]$ and $r_{SP}[\nu,\lambda]$, for the two incoming polarizations. We assume here that the contact area between the scatterer and the silver is very small compared to the contact area with air or vacuum, so we can model the interface as if it were between air or vacuum and silver:

$$r_{SN}[\nu,\lambda] = \frac{\cos[\nu] - (n_S[\lambda] + i\, k_S[\lambda])\cos[\eta]}{\cos[\nu] + (n_S[\lambda] + i\, k_S[\lambda])\cos[\eta]}$$

$$r_{SP}[\nu,\lambda] = \frac{\cos[\eta] - (n_S[\lambda] + i\, k_S[\lambda])\cos[\nu]}{\cos[\eta] + (n_S[\lambda] + i\, k_S[\lambda])\cos[\nu]},$$

where $n_S[\lambda]$ and $k_S[\lambda]$ are the real and imaginary indices of refraction of the silver as a function of wavelength. The intensity reflection coefficients can then be found by finding the magnitude squared of the amplitude reflection coefficients:

$$\begin{aligned} R_{SN}[\nu,\lambda] &= r_{SN}[\nu,\lambda] r_{SN}^*[\nu,\lambda] \\ R_{SP}[\nu,\lambda] &= r_{SP}[\nu,\lambda] r_{SP}^*[\nu,\lambda] \end{aligned}.$$

Each of these is then averaged over all incoming angles to find an average reflection coefficient for each polarization,

$$R_{SN}[\lambda] = (1/(2\pi))\int_0^{2\pi} d\phi \int_0^{\pi/2} R_{SN}[\nu,\lambda]\sin[\nu]\,d\nu = \int_0^{\pi/2} R_{SN}[\nu,\lambda]\sin[\nu]\,d\nu$$
$$R_{SP}[\lambda] = (1/(2\pi))\int_0^{2\pi} d\phi \int_0^{\pi/2} R_{SP}[\nu,\lambda]\sin[\nu]\,d\nu = \int_0^{\pi/2} R_{SP}[\nu,\lambda]\sin[\nu]\,d\nu \quad .$$

The total average reflectance, r_{Ag}, of silver is given by the average of these two reflection coefficients, assuming the scattered light is equally composed of both polarization components:

$$r_{Ag} = (R_{SN}[\lambda] + R_{SP}[\lambda])/2 \, .$$

The final result is only slightly different from the normal reflectivity of silver versus wavelength shown in Figure 18.

1.7 Second-Surface Mirror Theory

This section develops second-surface mirror theory so that it can be used to find the emissivity of the diffuse layer with a silver backing at long wavelengths where the diffuse layer looks like a continuous medium. The basic structure for this model is shown in Figure 25.

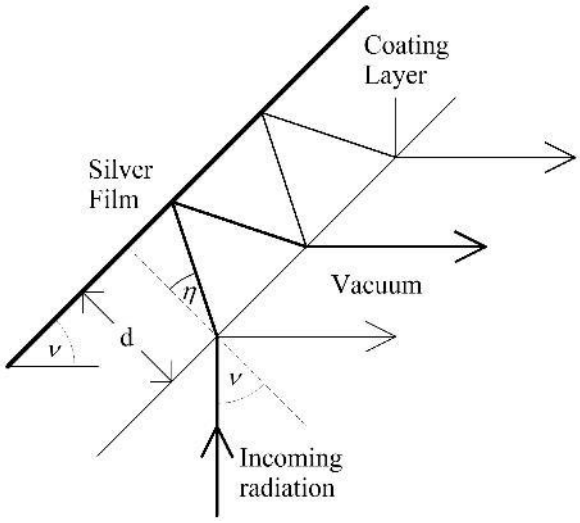

Figure 25. The multiple light paths taken by radiation impinging on a second-surface mirror oriented at an angle ν to the incoming solar radiation.

A few assumptions are needed before this entity can be analyzed:

1. The thickness of the coating layer, d, is much greater than the coherence length of the solar radiation. This removes the need to track amplitudes so that only intensities need to be analyzed, thereby reducing the difficulty substantially.
2. All radiation is spatially incoherent.
3. The incoming solar radiation is not polarized.

4. The analysis will only consider a small flat element of size dA. Extended objects will then be decomposed into a large number of small flat elements. It is assumed that the radius of curvature of these extended objects is very large compared to the thickness of the coating layer. This assumption allows light within the coating layer to propagate at the same angle after each reflection.
5. The coating layer is not birefringent.

When the incoming radiation hits the coating layer, it decomposes into two polarization states. Since the solar radiation is not polarized, half of the energy is assumed to be in each polarization state. Since it was assumed that there is no birefringence in the coating layer, each polarization state enters the coating layer at the same angle, η, given by Snell's law,

$$\sin[\eta] = \sin[\nu] / (n_B[\lambda] + i\, k_B[\lambda]),$$

where $n_B[\lambda]$ and $k_B[\lambda]$ are the real and imaginary indices of refraction for the mixed medium, composed of scattering material in air or vacuum. We have several mixing models to choose from when we deal with mixed medium. We have decided to use the Bruggeman model to find approximate relationships for the complex index of the scattering material [17].

Since the index of refraction is complex, the angle of propagation, η, is also complex. Physically this means that the wave in the coating material is inhomogeneous, meaning that it has a phase front along a plane that is different from the plane of constant amplitude.

The amount of light that reflects from the coating is given by the two reflection coefficients, $R_N[\nu,\lambda]$ and $R_P[\nu,\lambda]$. The subscripts *N* and *P* refer to the electric field being normal or parallel to the plane of incidence, i.e. the plane in which the light is traveling. The transmission coefficients, $T_N[\nu,\lambda]$ and $T_P[\nu,\lambda]$, are each equal to 1 minus the corresponding reflection coefficient by conservation of energy.

To find the reflection coefficients, we start with the Fresnel equations for the electric field reflection:

$$r_N[\nu,\lambda] = \frac{\cos[\nu] - (n_B[\lambda] + i\, k_B[\lambda])\cos[\eta]}{\cos[\nu] + (n_B[\lambda] + i\, k_B[\lambda])\cos[\eta]}$$

and

$$r_P[\nu,\lambda] = \frac{\cos[\eta] - (n_B[\lambda] + i\, k_B[\lambda])\cos[\nu]}{\cos[\eta] + (n_B[\lambda] + i\, k_B[\lambda])\cos[\nu]}.$$

The reflectance and transmittance coefficients are then given by

$$\begin{aligned} R_N[\nu,\lambda] &= r_N[\nu,\lambda] r_N^*[\nu,\lambda] \\ R_P[\nu,\lambda] &= r_P[\nu,\lambda] r_P^*[\nu,\lambda] \\ T_N[\nu,\lambda] &= 1 - R_N[\nu,\lambda] \\ T_P[\nu,\lambda] &= 1 - R_P[\nu,\lambda] \end{aligned},$$

where

$$\cos[\eta] = (1 - \sin[\eta]^2)^{1/2} = (1 - (\sin[\nu] / (n_B[\lambda] + i\, k_B[\lambda]))^2)^{1/2}.$$

This light travels into the coating material, losing energy, as described by the imaginary portion of the wave vector pointing into the material, $\mathrm{Im}[k_z]$. From Born and Wolf, section 13.2 [18], this transmission through the coating material is described by

$$T_C[\eta,\lambda] = \exp[-2(2\pi/\lambda)\,\mathrm{Im}[(n_B[\lambda]+i\,k_B[\lambda])\cos[\eta]]d] .$$

Then the light reaches the conducting layer, i.e. the silver, where a portion reflects and the remainder is absorbed. Letting $R_{SN}[\eta,\lambda]$ and $R_{SP}[\eta,\lambda]$ be the reflection coefficients from the silver for the two polarization states, the Fresnel equations yield

$$R_{SN}[\eta,\lambda] = \left[\frac{(n_B[\lambda]+i\,k_B[\lambda])\cos[\eta]-(n_S[\lambda]+ik_S[\lambda])\cos[\theta_S]}{(n_B[\lambda]+i\,k_B[\lambda])\cos[\eta]+(n_S[\lambda]+ik_S[\lambda])\cos[\theta_S]}\right]\left[\frac{(n_B[\lambda]+i\,k_B[\lambda])\cos[\eta]-(n_S[\lambda]+ik_S[\lambda])\cos[\theta_S]}{(n_B[\lambda]+i\,k_B[\lambda])\cos[\eta]+(n_S[\lambda]+ik_S[\lambda])\cos[\theta_S]}\right]^*$$

$$R_{SP}[\eta,\lambda] = \left[\frac{(n_B[\lambda]+i\,k_B[\lambda])\cos[\theta_S]-(n_S[\lambda]+ik_S[\lambda])\cos[\eta]}{(n_B[\lambda]+i\,k_B[\lambda])\cos[\theta_S]+(n_S[\lambda]+ik_S[\lambda])\cos[\eta]}\right]\left[\frac{(n_B[\lambda]+i\,k_B[\lambda])\cos[\theta_S]-(n_S[\lambda]+ik_S[\lambda])\cos[\eta]}{(n_B[\lambda]+i\,k_B[\lambda])\cos[\theta_S]+(n_S[\lambda]+ik_S[\lambda])\cos[\eta]}\right]^*,$$

where θ_S is the angle of the light propagation in the silver and is given by another application of Snell's law, i.e.

$$\sin[\theta_S] = (n_B[\lambda]+i\,k_B[\lambda])\sin[\eta]/(n_S[\lambda]+i\,k_S[\lambda]) .$$

The goal is to calculate the amount of energy that is lost inside of the selective coating to absorption by the coating or by the silver. We start by considering the first pass of light through the coating, reflecting off of the silver and then passing through the coating again. The light lost during this first pass, $A_{1N}[\nu,\lambda]$, is given by

$$A_{1N}[\nu,\lambda] = T_N[\nu,\lambda](1-T_C[\nu,\lambda]^2 R_{SN}[\eta,\lambda]) .$$

The quantity in parentheses is 1 minus the fractional amount of light that made it through one circuit, i.e. the fractional amount lost during one round trip. The $T_N[\nu,\lambda]$ coefficient is the amount of light that refracted into the coating layer.

So, an amount of light given by $T_N[\nu,\lambda]T_C[\nu,\lambda]^2 R_{SN}[\eta,\lambda]$ makes it back to the surface of the selective coating. At this point, it reflects off of the surface, i.e. a portion given by $R_N[\nu,\lambda]$ reflects back into the selective surface to start the next round trip cycle. So the amount of light lost during the next circuit, $A_{2N}[\nu,\lambda]$, is given by

$$A_{2N}[\nu,\lambda] = T_N[\nu,\lambda]T_C[\nu,\lambda]^2 R_{SN}[\eta,\lambda]R_N[\nu,\lambda](1-T_C[\nu,\lambda]^2 R_{SN}[\eta,\lambda]) .$$

Generalizing this, the amount of light lost during pass i is given by

$$A_{iN}[\nu,\lambda] = T_N[\nu,\lambda](T_C[\nu,\lambda]^2 R_{SN}[\eta,\lambda]R_N[\nu,\lambda])^{i-1}(1-T_C[\nu,\lambda]^2 R_{SN}[\eta,\lambda]) .$$

The total light absorbed is the sum of all of these terms, i.e.

$$A_N[\nu,\lambda] = \sum_{i=1,\infty} A_{iN}[\nu,\lambda] = \sum_{j=0,\infty} T_N[\nu,\lambda](T_C[\nu,\lambda]^2 R_{SN}[\eta,\lambda]R_N[\nu,\lambda])^j(1-T_C[\nu,\lambda]^2 R_{SN}[\eta,\lambda]) ,$$

which can be reexpressed as

$$A_N[\nu,\lambda]=\frac{T_N[\nu,\lambda](1-T_C[\nu,\lambda]^2R_{SN}[\eta,\lambda])}{1-T_C[\nu,\lambda]^2R_{SN}[\eta,\lambda]R_N[\nu,\lambda]}=\frac{(1-R_N[\nu,\lambda])(1-T_C[\nu,\lambda]^2R_{SN}[\eta,\lambda])}{1-T_C[\nu,\lambda]^2R_{SN}[\eta,\lambda]R_N[\nu,\lambda]}.$$

The parallel polarization absorption can be found in the same fashion:

$$A_P[\nu,\lambda]=\frac{T_P[\nu,\lambda](1-T_C[\nu,\lambda]^2R_{SP}[\eta,\lambda])}{1-T_C[\nu,\lambda]^2R_{SP}[\eta,\lambda]R_P[\nu,\lambda]}=\frac{(1-R_P[\nu,\lambda])(1-T_C[\nu,\lambda]^2R_{SP}[\eta,\lambda])}{1-T_C[\nu,\lambda]^2R_{SP}[\eta,\lambda]R_P[\nu,\lambda]}.$$

The goal of this section was to find the absorption of a second-surface mirror as a function of wavelength and angle. That parameter, $A[\nu,\lambda]$, is simply the average of the two polarization absorption parameters shown above:

$$A[\nu,\lambda]=(A_P[\nu,\lambda]+A_N[\nu,\lambda])/2.$$

1.8 Complete Model

The preceding sections have developed expressions for the amount of energy that is absorbed by the diffuse selective surface as a function of angle and wavelength. Recalling that the fractional absorption is also the emissivity, we are now in a position where the total solar energy absorbed by the surface can be calculated and where the total emitted IR energy can be found. Equating these two energies then determines the temperature of the surface. In addition, we can find the temperature of more complicated entities, for example, cylinders and spheres, by decomposing them into small flat elements and calculating the total solar energy absorptance and IR emittance.

Summarizing the key equations:

a. The wavelength λ_C, where the model transitions between a diffuse scattering model and a second-surface mirror model, is determined. We have decided to set this transition to the wavelength where the total thickness of the diffuse material equals one scattering length, i.e.

$$d=3a/s[\lambda_C],$$

where d is the coating thickness and $s[\lambda]$ is given by

$$s[\lambda]=\frac{2f^{1/3}}{3a}\frac{289}{25}\left|\frac{\tilde{n}^2-1}{\tilde{n}^2+2}\right|^2\frac{1+3/(1+(1-10a/(3\lambda))^2)}{1+(3\lambda/(10a))^4}.$$

b. For wavelengths less than λ_C, the selective surface can be modeled as a diffuse scatterer with a silver backing. In this regime, the fractional power absorbed by light impinging normal to the surface is given by

$$A[\lambda]=1-\frac{2r_{Ag}\sqrt{\kappa(\kappa+s)}\cosh[d\sqrt{\kappa(\kappa+s)}]+(s-r_{Ag}(2\kappa+s))\sinh[d\sqrt{\kappa(\kappa+s)}]}{2\sqrt{\kappa(\kappa+s)}\cosh[d\sqrt{\kappa(\kappa+s)}]+(2\kappa+s-r_{Ag}s)\sinh[d\sqrt{\kappa(\kappa+s)}]}.$$

r_{Ag} is an averaged reflectivity of silver (the expressions for this were shown earlier and will not be repeated here). κ is a loss parameter, which is related to the material's imaginary index of refraction, $k[\lambda]$, by the relation

$$\kappa = 12\pi k[\lambda] f / \lambda ,$$

where f is a fill factor. So the absorption, $A[\lambda]$, is a function of wavelength due to varying material properties and changes in scattering properties with wavelength.

c. For wavelengths longer than λ_C, the selective surface can be modeled as a second-surface mirror and the absorption is given by

$$A[\nu,\lambda] = (A_P[\nu,\lambda] + A_N[\nu,\lambda]) / 2 ,$$

where the absorption expressions for the two different polarization states are given in the preceding section and will not be repeated here.

The three steps above provide expressions for the absorption of the selective surface as a function of wavelength and, for the second-surface mirror, as a function of incoming angle. The next step is to calculate the amount of solar energy absorbed. Let $I_S[\lambda]$ be the solar irradiance density. If a flat plate coated with the selective surface is tilted at an angle ν relative to the incoming sunlight, then the total power density absorbed on the plate, $A_{tot}[\nu]$, will be

$$A_{tot}[\nu] = \int I_s[\lambda] A[\nu,\lambda] \cos[\nu] d\lambda = \cos[\nu] \int I_s[\lambda] A[\nu,\lambda] d\lambda .$$

Multiplying this by the plate area yields the total watts absorbed by the plate.

The next step is to calculate the total power density emitted by the plate. From Kirchhoff's law, the emissivity of a surface is equal to its absorption, and we have expressions for the absorption, $A[\nu,\lambda]$, as a function of angle from normal and wavelength. Using this, the total energy emitted by the surface can be found. We start with Planck's law written in terms of wavelength, i.e.

$$P_\lambda[\lambda,T] = \frac{2hc^2}{\lambda^5} \frac{1}{\exp[\frac{hc}{\lambda kT}] - 1} ,$$

where h is Planck's constant, c is the speed of light, and k is the Boltzmann constant. This equation provides the watts emitted by a surface into a given steradian-per-unit wavelength and per-unit area assuming a perfect blackbody. In order to find the total power-per-unit area emitted by a surface, $P[T]$, this expression is multiplied by the emissivity of the surface, which is equal to the absorption, and then integrated over the hemisphere (2π steradians) with a cosine term added to account for the projected area of the emitting surface and over all wavelengths:

$$P[T] = 2\pi \int_0^\infty \int_0^{\pi/2} \frac{2hc^2}{\lambda^5} \frac{A[\nu,\lambda]}{\exp[\frac{hc}{\lambda kT}] - 1} \cos[\nu] \sin[\nu] d\nu d\lambda .$$

Finally, to find the steady-state temperature of an object in deep space being irradiated by the Sun, the energy absorbed has to equal the energy emitted. The analysis above provides expressions for the solar energy absorbed by a flat plate oriented at an angle, ν, relative to the Sun direction and for the energy emitted. If the plate can only emit energy from the illuminated surface (this would be the case if the plate were a small piece of a larger, closed-shell object, where the back side faces other portions of the same object), then the steady-state temperature is found by solving

$$P[T] = A_{tot}[\nu].$$

If the plate has two surfaces from which to radiate, this equation becomes

$$2P[T] = A_{tot}[\nu].$$

If we assume the object to be a long cylinder (such that we can ignore the ends) and we assume the cylinder's axis to be perpendicular to the direction to the Sun, with radius R and length L, then the object will radiate a total energy given by its area times $P[T]$ and will absorb energy over each differential element facing the Sun. Equating these two energies yields

$$P[T]2\pi RL = \int_0^L \int_{-\pi/2}^{\pi/2} A_{tot}[\nu] R d\nu dx = RL \int_{-\pi/2}^{\pi/2} A_{tot}[\nu] d\nu$$
$$2\pi P[T] = \int_{-\pi/2}^{\pi/2} A_{tot}[\nu] d\nu \quad \text{or} \quad \pi P[T] = \int_0^{\pi/2} A_{tot}[\nu] d\nu .$$

If the object is assumed to be a sphere with radius R, then the object will radiate a total energy given by its area times $P[T]$ and will absorb energy over each differential element facing the Sun. Equating these two energies yields

$$P[T]4\pi R^2 = \int_0^{2\pi} \int_0^{\pi/2} A_{tot}[\nu] R^2 \sin[\nu] d\nu d\phi = 2\pi R^2 \int_0^{\pi/2} A_{tot}[\nu] \sin[\nu] d\nu$$
$$2P[T] = \int_0^{\pi/2} A_{tot}[\nu] \sin[\nu] d\nu .$$

We solve these equations numerically, and the results are shown in Section 1.9.

1.9 Theoretical Results

We have decided to model seven materials—MgF_2, CaF_2, BaF_2, CsBr, KCl, NaCl, and KBr—based on the discussion in Section 1.3. For each of these and the remainder of the report, we have set the particle size to 0.25 µm and the fill factor, f, to 0.3. These are not critical parameters for achieving cryogenic temperatures in that their primary purpose is to set the thickness of the diffuse coating. In other words, if we change the fill factor or the particle size, or decide the scattering length function should be modified, the surface will still reach cold temperatures, but the necessary thickness will change. However, changing these also alters the emission characteristics, so changing them would require running the modeling software again to obtain new predicted temperatures.

For each material, we determined the temperature that a two-sided 1 m^2 plate (oriented to face the Sun), a 1 m-long and 1 m-radius cylinder (oriented with its axis perpendicular to the direction to the Sun), and a 1 m-radius sphere would reach if coated with silver and then a diffuse coating of material at varying thickness. We assume that the cylinder has no emission from its ends so that the results can be extended to wires and other cylindrical objects without ends.

Table 2 shows the power absorbed/emitted (i.e. equilibrium) and resulting temperature for each geometry exposed to full sunlight in deep space (1 AU from the Sun and far from the Earth-Moon) for a 5 mm coating of each material. Detailed results for each material are shown on the following pages, but this table highlights the relative performance. Note that spheres reach a lower temperature than cylinders, which is lower than that reached by the plates, because the spheres have a larger ratio of emitting area to absorption cross section area than that of the cylinders, which is larger than that of the plates. The power values shown vary primarily due to the different cross-sectional sizes of each object. The plate has a 1 m^2 cross section, the cylinder has a 2 m^2 cross section, and the sphere has a π m^2 cross section; and these factors strongly determine the relative powers shown in the table. This result correlates with the weak angular dependence on the emissivity predicted by the models above.

Table 2. Power absorbed/emitted and corresponding equilibrium temperatures for a two-sided plate, a cylinder, and a sphere exposed to full sunlight in deep space (1 AU) for seven different coating materials at 5 mm thickness.

Material	Two-Sided Plate		Cylinder		Sphere	
	Power (W)	Temp (K)	Power (W)	Temp (K)	Power (W)	Temp (K)
BaF_2	1.04	61.5	2.12	56.0	3.35	53.3
CaF_2	2.15	71.9	4.29	64.9	6.72	61.5
MgF_2	2.61	74.9	5.32	68.0	8.43	64.6
NaCl	0.73	56.9	1.47	51.9	2.32	49.5
KCl	0.73	56.7	1.46	51.7	2.31	49.3
KBr	0.66	55.7	1.32	50.7	2.07	48.3
CsBr	0.59	56.8	1.19	51.0	1.87	48.6

The amount of power absorbed, as will be discussed, depends strongly on the IR absorption of the coating. The final equilibrium temperatures depend primarily on this absorption and on the far-IR emissivity of the coatings.

1.9.1 Absorbed Power and Equilibrium Temperature

The following unnumbered plots expand on the results in Table 2 by showing how the absorbed power and the equilibrium temperature vary for these seven materials and three geometries as the thickness of the coating varies from 0.5 mm to 10 mm. Note that the isotropic scattering distance in the visible portion of the spectrum is about 0.5 µm, so even a 0.5 mm-thick coating has 1000 scattering lengths. From Equation 9, even if the silver reflects only 94% of the light, the coating will reflect 99.9%. So even the 0.5 mm-thick layers reflect much of the solar spectrum and can achieve cryogenic temperatures.

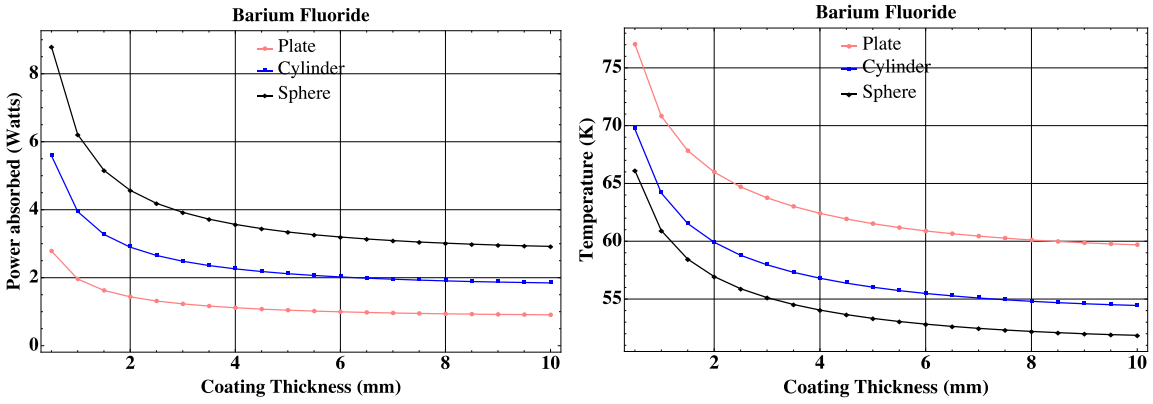

BaF_2 plots of absorbed power and equilibrium temperature versus coating thickness for a plate, cylinder, and sphere.

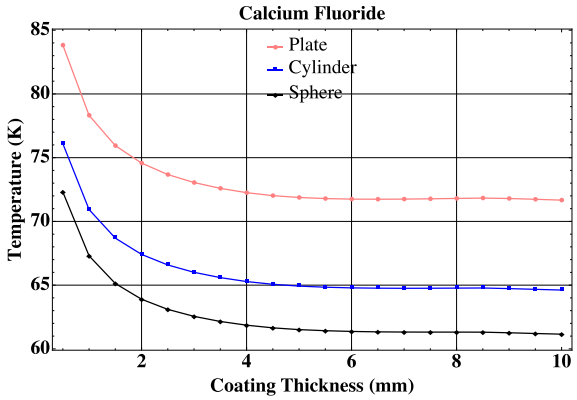

CaF_2 plots of absorbed power and equilibrium temperature versus coating thickness for a plate, cylinder, and sphere.

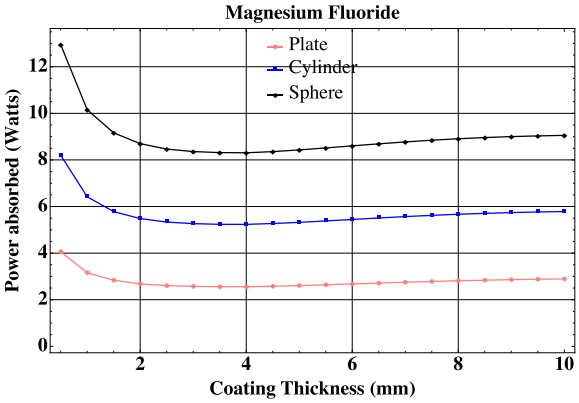

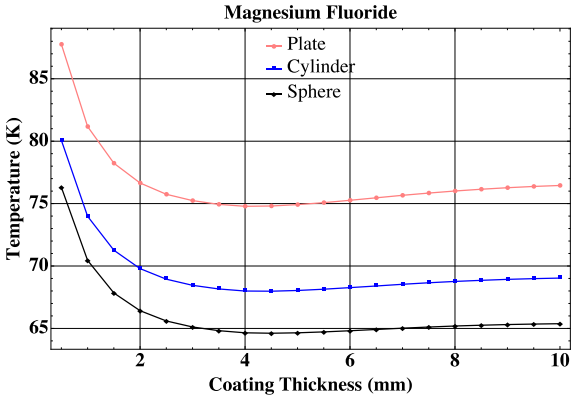

MgF_2 plots of absorbed power and equilibrium temperature versus coating thickness for a plate, cylinder, and sphere.

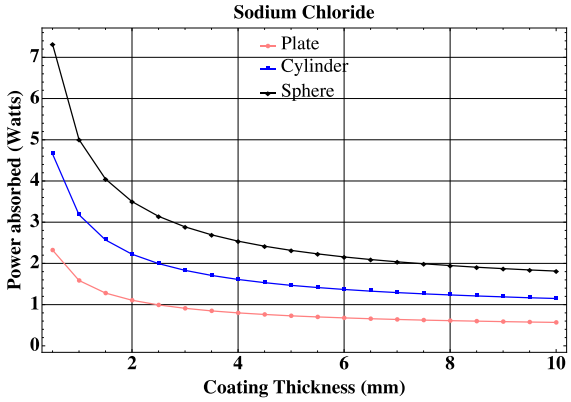

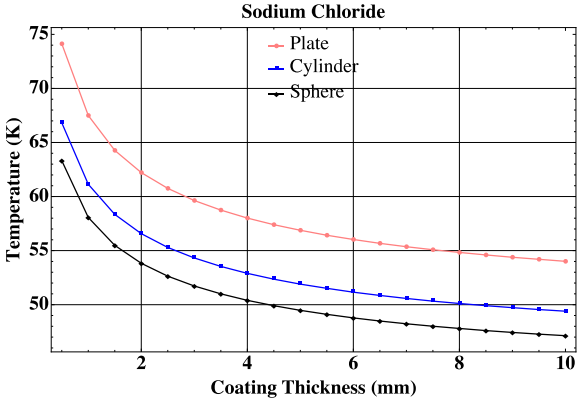

NaCl plots of absorbed power and equilibrium temperature versus coating thickness for a plate, cylinder, and sphere.

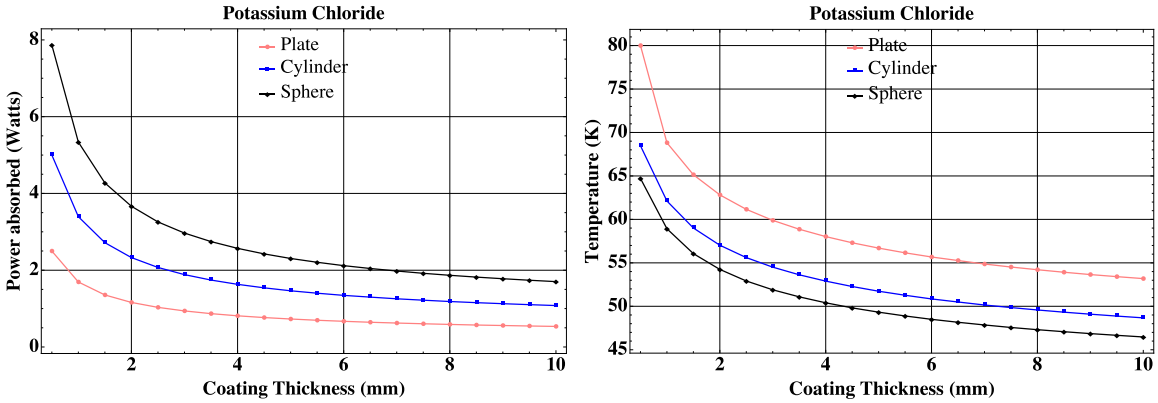

KCl plots of absorbed power and equilibrium temperature versus coating thickness for a plate, cylinder, and sphere.

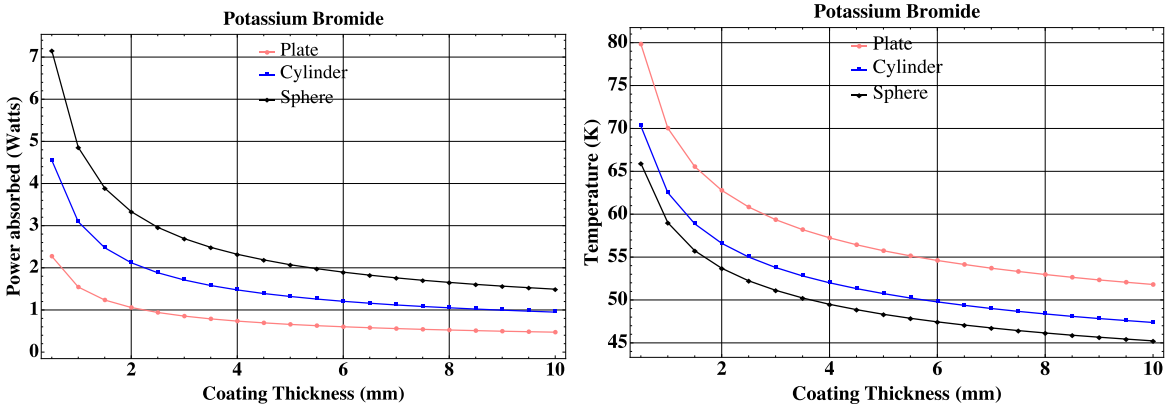

KBr plots of absorbed power and equilibrium temperature versus coating thickness for a plate, cylinder, and sphere.

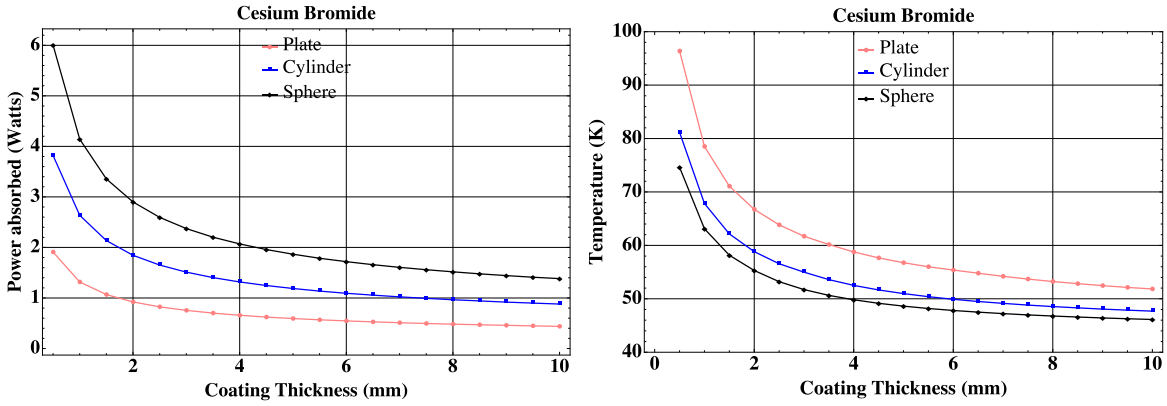

CsBr plots of absorbed power and equilibrium temperature versus coating thickness for a plate, cylinder, and sphere.

We limited the plots above to 1 cm maximum thickness, but some are still sloping downward for that thickness. So we decided to try a much thicker coating to see what the predicted limit was for power absorbed and temperature. After considering several materials we chose to model a sphere coated with a thick layer of KBr because it had the best combination of IR characteristics. A minimal temperature just below 40 K is predicted, the lowest achieved in our models. This amazing result will be discussed in more detail below when the plots for spectral power absorbed and emitted are shown.

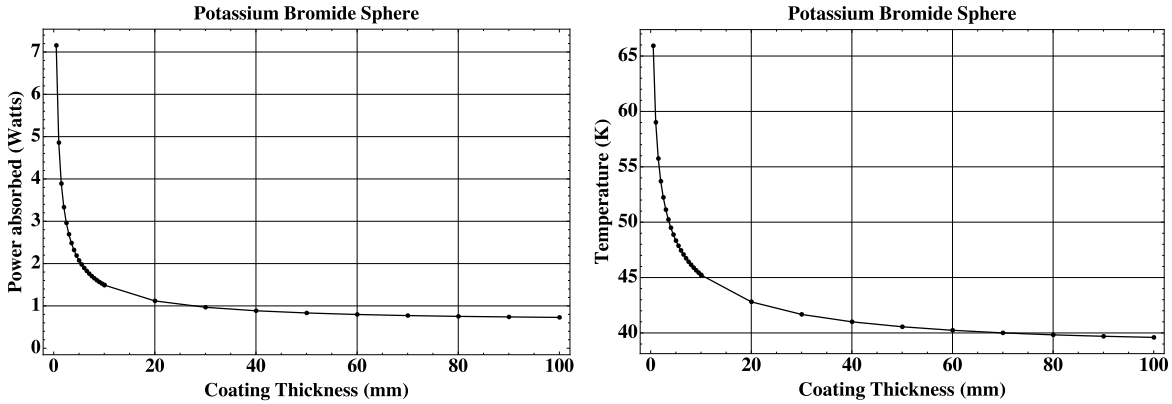

KBr plots of absorbed power and equilibrium temperature versus coating thickness for a sphere with coating thickness reaching 100 mm. This plot shows the lowest temperature achieved in our models, just below 40 K.

1.9.2 Absorbed and Emitted Spectral Power

The following unnumbered plots show the power absorption spectrum and the power emission spectrum for each of the seven materials for a two-sided plate coated on both sides with a 5 mm layer of Solar White with normal solar irradiance (additional BaF_2 and KBr plots are shown with a 40 mm of coating). In addition, the normal emissivity as derived by our model is shown, and in each case, the equilibrium temperature of the plate is shown in the caption. These curves supply significant insight into the physics behind the operation of the coatings.

Each curve shows three plots: the spectral density of the absorbed power (black), the spectral density of the emitted power (pink), and the normal emittance as predicted by the models (blue). The area under the emittance plot times 2 (the plate emits from two sides) equals the area under the absorbed power plot. This may not be immediately obvious since the wavelength axis is logarithmic.

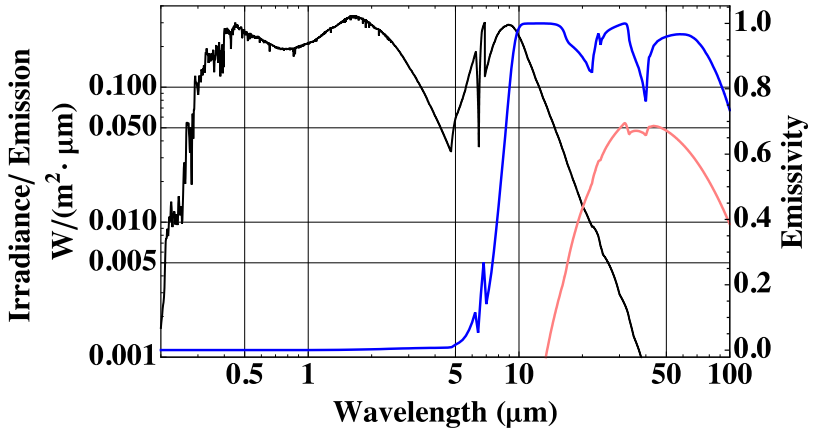

MgF_2 absorbed and emitted spectral power curves and normal emissivity for 74.9 K and 5 mm-thick coating.

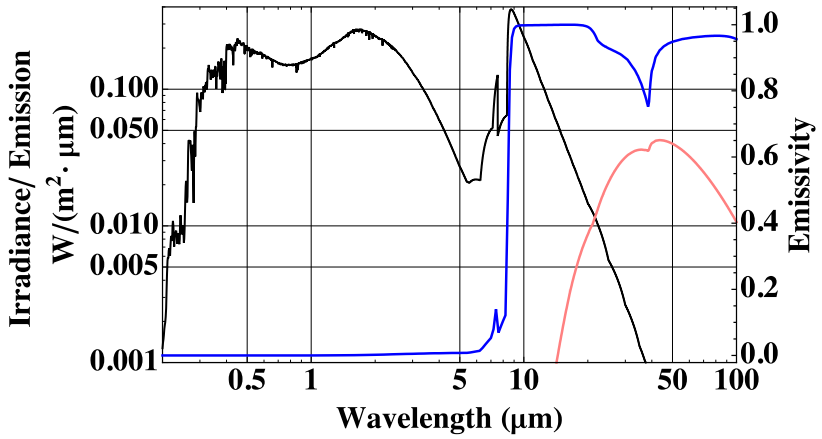

CaF_2 absorbed and emitted spectral power curves and normal emissivity for 71.9 K and 5 mm-thick coating.

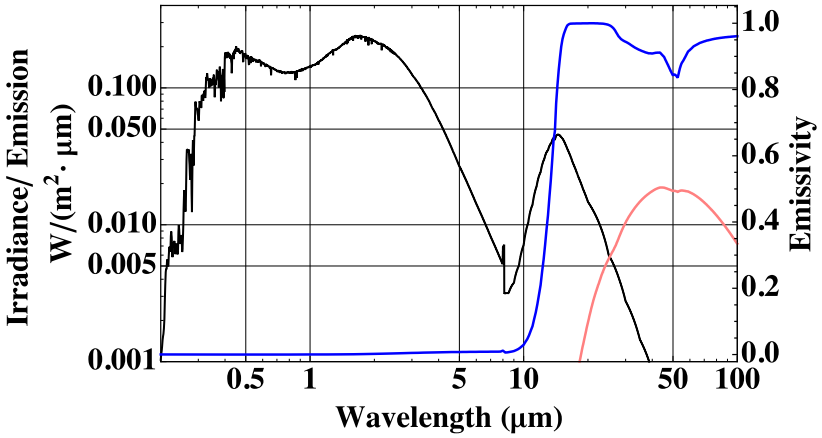

BaF_2 absorbed and emitted spectral power curves and normal emissivity for 61.5 K and 5 mm-thick coating.

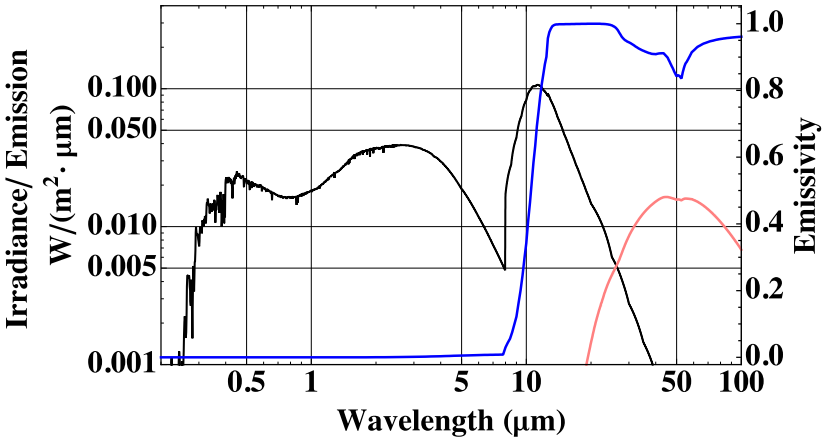

BaF_2 absorbed and emitted spectral power curves and normal emissivity for 60 K and 40 mm-thick coating.

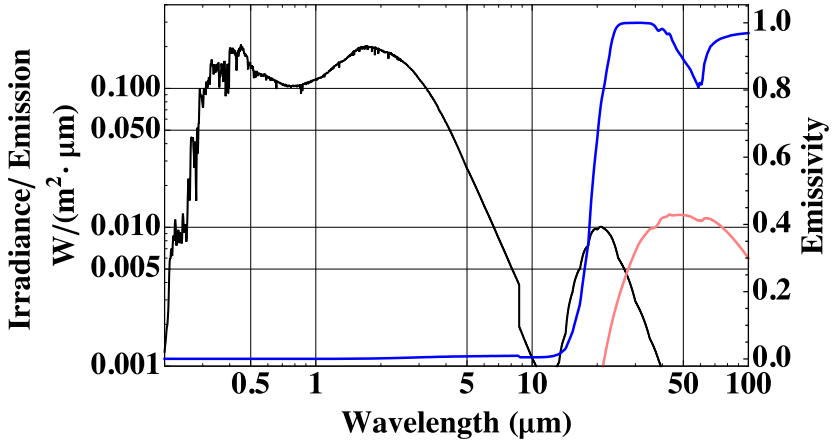

NaCl absorbed and emitted spectral power curves and normal emissivity for 56.9 K and 5 mm-thick coating.

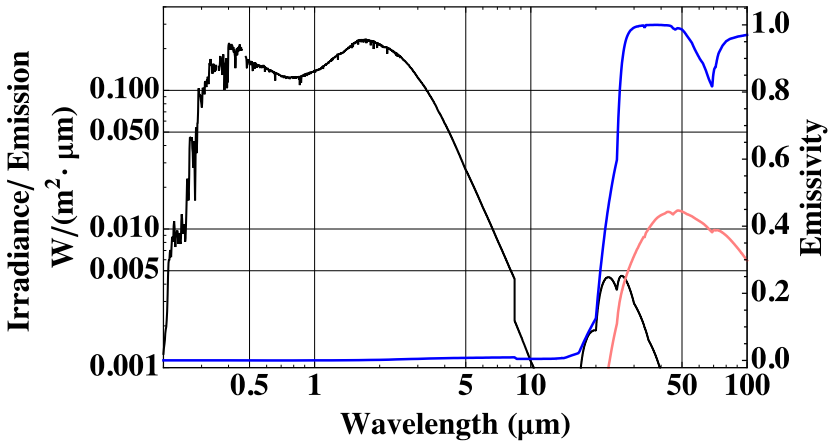

KCl absorbed and emitted spectral power curves and normal emissivity for 56.7 K and 5 mm-thick coating.

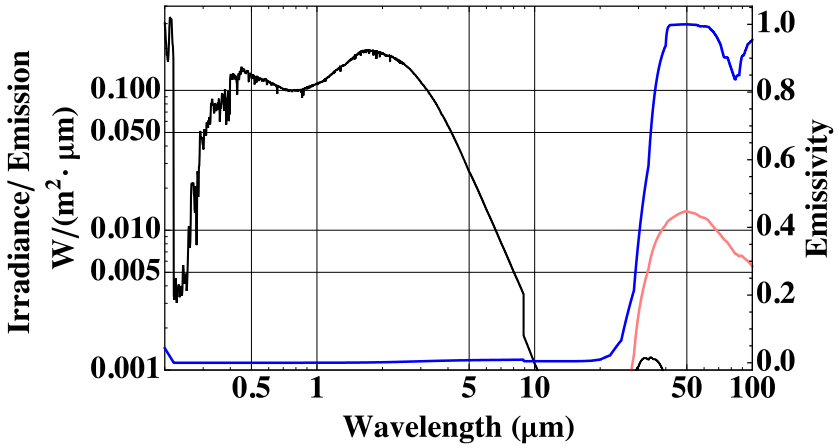

KBr absorbed and emitted spectral power curves and normal emissivity for 55.7 K and 5 mm-thick coating.

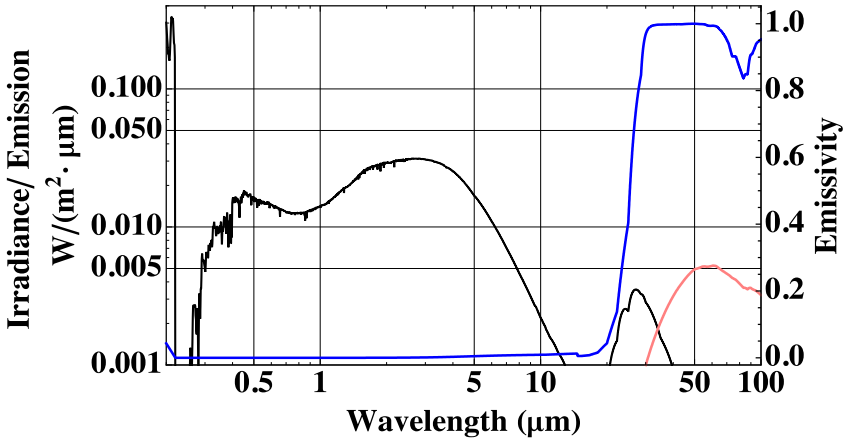

KBr absorbed and emitted spectral power curves and normal emissivity for 46.6 K and 40 mm-thick coating.

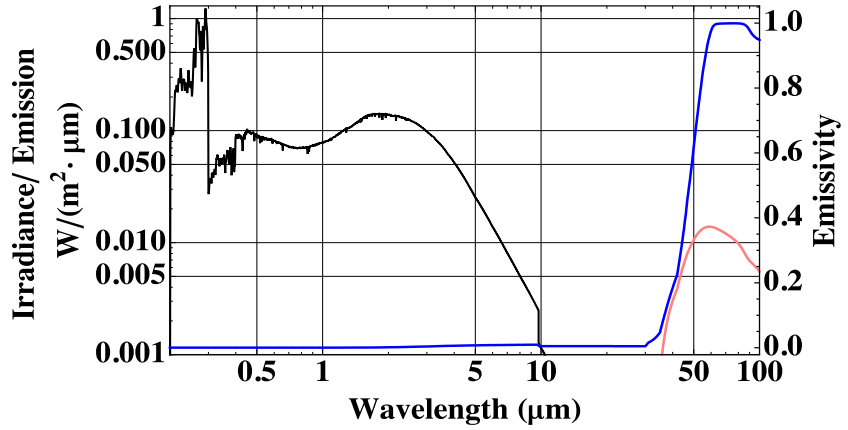

CsBr absorbed and emitted spectral power curves and normal emissivity for 56.8 K and 5 mm-thick coating.

In each 5 mm-thick coating case, there are roughly $N = 1000$ scattering layers in the material in the visible region of the spectrum, implying from Equation 9 that 0.0001 of the incoming energy is absorbed. So the absorbed solar energy, shown as the black line in the plots, should be roughly 0.0001 of the Sun's irradiance in the visible. From the solar spectral irradiance model cited early in this report, the Sun's peak irradiance in the visible region is about 2000 W/(m^2 · μm). These plots show that the absorbed power in the visible region of the spectrum is about 0.2 W/(m^2 · μm), i.e. a reduction of about 0.0001. The fact that this approximation is so close to the prediction of the full model increases the confidence of the model. Now consider the 40 mm-thick coating cases. The Sun's energy across the low-emissivity region should be reduced by an additional factor of about 40/5 = 8. The two 40 mm-thick coatings indeed show a drop of about this magnitude.

In all of the plots, the absorbed solar spectral irradiance is roughly flat from the visible out to about 2 μm and then starts to fall rapidly. Through the visible and near-IR regions, the solar energy drops slowly while the scattering length gets longer and the reflectivity of the silver improves. These effects apparently balance until about 2 μm, when the rapid fall in the solar spectral irradiance dominates, resulting in a drop in the absorbed energy.

Now consider the blue emissivity curve. When this curve begins to increase, it indicates that the coating will start to absorb solar energy, so the absorbed power curve begins to rise with the emissivity. The curves are ordered by the wavelength where the emissivity curves starts to rise. MgF_2 is first and begins to absorb at about 5 μm, causing a significant IR absorption, which yields the highest temperature of any of the materials. Adding more MgF_2 will reduce the visible/near-IR absorption, but the mid to far absorption will grow faster, resulting in an increase in

temperature (as seen in the coating thickness plots a few pages back). Looking down the plots at the 5 mm-thick coating cases, the amount of IR absorption drops for each case due to the shift in emissivity for longer wavelengths.

So CsBr appears to be ideal in the infrared since its far-IR absorption is so small that it doesn't even appear on the plot. However, the long-wave emissivity makes it difficult for CsBr to emit radiation (its emission curve runs into the emissivity plot), and CsBr has absorption in the ultraviolet. So KBr is a better material, and we decided to model a 40 mm-thick coating of it (both the 5 mm- and 40 mm-thick coating cases for KBr are shown above). KBr has a small UV absorption peak, but increasing the coating thickness does not change this much, indicating that 5 mm was sufficient to absorb the solar energy there. The visible-mid-IR absorption drops by about the predicted factor of 8, and the far-IR absorption has grown when comparing the 40 mm coating to the 5 mm coating. But the far-IR absorption increase does not offset the visible-near-IR decrease, so the absorbed power drops substantially and the plate temperature drops from 55.7 K to 46.6 K. As shown in the varying thickness plots, the temperature continues to drop even out to thicknesses of 80 mm to 100 mm, and then there is more drop from the plate to the sphere, resulting in a prediction below 40 K.

Note that each plot has a far-IR emission curve that is roughly a composite of the Planck spectral emission curve for the plate temperature times the emissivity curve. The far-IR emissivities of these materials all approach 1 over selected regions because they have small real indices, which are made smaller by the presence of vacuum space, resulting in minimal surface reflection.

In all of the plots, the absorption/emission models have a discontinuity where we switch from a scattering model to a second-surface mirror model. This happens when the isotropic scattering distance equals the coating thickness. For the 5 mm coatings, this happens between wavelengths of 7 μm and 10 μm.

1.9.3 Emissivity vs. Temperature

In all of the discussion to this point, the emissivity is presented as a function of wavelength, but in much of the literature, emissivity is spoken of as a function of temperature. We can convert the wavelength-dependent emissivity into a temperature-dependent emissivity by placing a perfect blackbody at some temperature, T, far from a Solar White-coated object. We can then determine the total amount of energy absorbed by the coated object and compare this with the total power impinging on the object. For a sphere, the mathematical expression is

$$\langle \varepsilon \rangle = \frac{\int_0^{2\pi}\int_0^{\pi/2}\left(\int \frac{4\pi hc^2 A[\nu,\lambda]}{\lambda^5 \exp[\frac{hc}{\lambda kT}]-1}\cos[\nu]\,d\lambda\right)R^2\sin[\nu]\,d\nu\,d\phi}{\int_0^{2\pi}\int_0^{\pi/2}\left(\int \frac{4\pi hc^2}{\lambda^5 \exp[\frac{hc}{\lambda kT}]-1}\cos[\nu]\,d\lambda\right)R^2\sin[\nu]\,d\nu\,d\phi}.$$

This expression is plotted in Figure 26 for three spherical cases: one coated with a 5 mm layer of Solar White composed of KBr on silver, one with 5 mm of Solar White composed of BaF_2 on silver, and the last with 5 mm of Solar White composed of CsBr on silver. Note that all have nearly unit emissivity for cold objects because they have high absorption at long wavelengths. All drop as the temperature goes up and reach minimums near the solar-effective temperature of 5778 K. The last points for the KBr and CsBR curves start to come back up again due to high-temperature (above 6000 K) objects emitting radiation in their UV absorption bands. If the curve went higher in temperature, the BaF_2 would begin to turn upward as well. Each material coating has an average emissivity around 0.001 for solar-temperature objects, indicating the high effective rejection of solar energy. Each radiates well at low temperatures, being nearly perfect blackbodies at cryogenic temperatures.

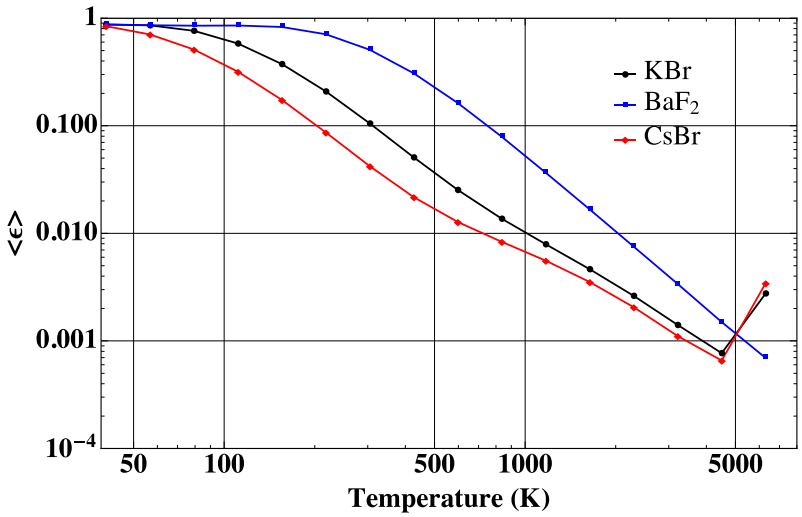

Figure 26. Average emissivity versus temperature for 5 mm of KBr, 5 mm of BaF_2, and 5 mm of CsBr on silver on a sphere.

1.10 Experimental Results

We have not yet tested our coatings in an appropriate test chamber to verify the theoretical models, but we have performed limited optical testing. We ground NaCl into a very fine powder by placing high-grade salt into a grinder for 3 minutes. Then, using a press, we created several 20 mm-diameter, 1.1 mm-thick disks. One disk, limited to 5 MPa pressure, had some structural integrity, yet still looked like a white diffusive material as shown in Figure 27. It weighed 0.66 g, so its density is 1.89 g/cm^2. Solid salt is 2.17 g/cm^2, so it is 87% salt and only 13% air. This is probably not optimal, based on our paint studies, and we will work to improve on this.

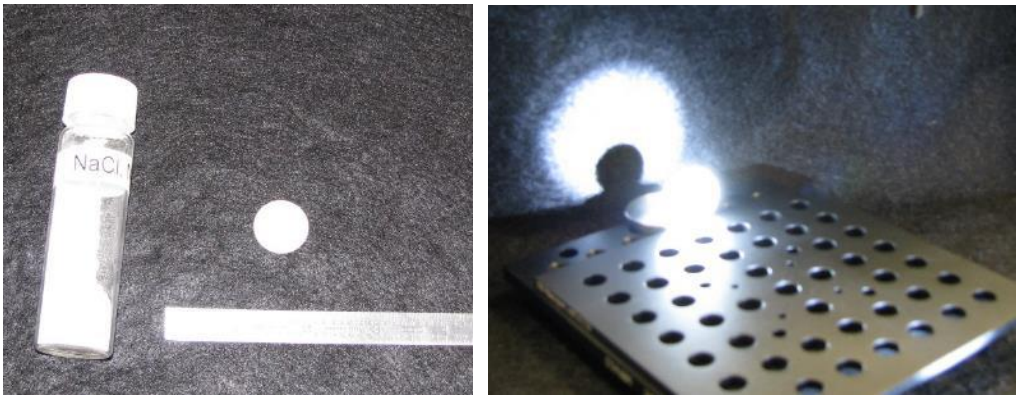

Figure 27. Optical testing with NaCl. The image on the left shows finely ground NaCl, along with a 20 mm-diameter, 1 mm-thick pressed disk of NaCl powder. The image on the right shows the reflecting ability of this thin layer of NaCl powder.

We directed a light source at this disk and found that it had about 5% transmission in the visible range. Now, we didn't grind the salt very long, so it might be reasonable to assume that the particle size is about 10 μm. This means the scattering length is about 30 μm (since the particles are large compared to a wavelength), so there are about 37 scattering layers. The predicted transmission is then given by 2/(number of layers + 2) = 2/39 = 5%. The agreement between measurement and theory is somewhat coincidental, but indicates that we might have a reasonable physical model of what is going on.

2. OVERVIEW OF CRYOGENIC LOX STORAGE ON A MARS MISSION

An important part of a NIAC project is to show the impact of a concept on a mission. In our proposal, we proposed two different mission impacts to study: one was the long-term storage of LOX on a mission to Mars, and the other was the generation of a large-scale superconducting galactic cosmic ray (GCR) shield. When our Phase I proposal was accepted, we were asked to drop the GCR shield and concentrate only on the Mars LOX storage issue. With current technology it is not possible to maintain LOX in deep space for more than a few days [19, 20].So that is the mission concept we have addressed and describe in this second section of the report.

We will start by presenting a very simple model of the region around a LOX tank on a Mars mission vehicle, since we do not have the resources to examine a detailed vehicle design. Studying a simplified version presents the issues, showcases the analysis, and demonstrates the impact of the Solar White coating. After presenting the vehicle configuration, we will discuss the energy budget, i.e. we will present the relationship between the total power absorbed by a spherical LOX tank and its temperature in order to show how much energy can be absorbed through different mechanisms while still maintaining liquid oxygen. Of course, the goal is to keep the LOX as cold as possible to minimize the pressure and the tank wall thickness needed to keep it liquid. Figure 28 shows the pressure necessary to keep LOX liquid at different temperatures, and clearly, there is a significant advantage to keeping the LOX in the 70 K to 80 K range than at 90 K (recall that 0.1 MPa is about 1 atm).

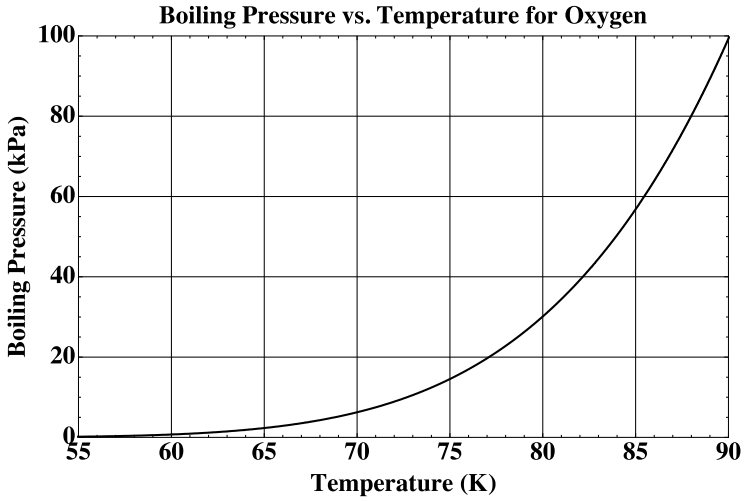

Figure 28. Boiling pressure versus temperature for oxygen.

After presenting the energy budget, we model four routes by which heat can reach the LOX tank in a vehicle configuration, in addition to the direct solar radiation modeled above: planetary radiation, reflected radiation, radiation from the other vehicle components, and heat conduction along support struts and the feed line. Each of these will be discussed in some detail, trying to determine relative impacts and restrictions. For example, it will be shown that the IR emission from the Earth on a vehicle in low Earth orbit is excessive and prevents the long-term storage of LOX, but at higher altitude orbits this heat load can be tolerated.

After the sources of heat are modeled and calculated, they can be summed to determine the total heat load on the LOX tank, and we can determine the conditions and design space that allow long-term storage of LOX on a Mars mission. The conclusion of this work will show, assuming some design considerations are accepted, that the use of a Solar White coating will allow LOX to be maintained on a long-duration mission to Mars.

2.1 Assumed LOX Tank Mission Architecture

In order to determine the temperature that a LOX tank will reach on a mission to Mars, one must model the emission and reflectance of all significant objects within the field of view of the LOX tank and determine the heat conducting along all significant connections to the LOX tank. At present, there is no definitive Mars vehicle, so a detailed analysis cannot be performed. However, for the purposes of this study, we only need a simplified design in order to analyze the primary heat load paths to the LOX tank. The subsequent analysis will then indicate how these results would vary if the vehicle design were modified.

For the purposes of this study, we are proposing that the region around the LOX tank for a Mars mission vehicle could look like the sketch in Figure 29. We're assuming a spherical, 4 m-diameter LOX tank coated in Solar White located between similar-size spherical structures. The structure to the left is a fuel tank (though it might also be living quarters), but for the purpose of the model its purpose is not important. We only need to know that the LOX tank is located 1 m from it, that it is 4 m in diameter, that the LOX tank only sees exposed metal (e.g. aluminum) on it, and that it is maintained at a temperature of 300 K. Note that there can be additional substantial vehicle components to the left of this structure, but as long as they are out of the view of the LOX tank, they do not affect the analysis. Likewise, structures such as a fuel line and cabling are assumed to have cross-sectional areas small enough to exert only a minimal heat load on the LOX tank. We further assume that the fuel tank contains something akin to kerosene and must be kept at about 300 K, though of course, if the fuel tank contained liquid methane at say 100 K, then the heat load from this entity would be much lower. So, we are assuming a worst case.

On the right side of the LOX tank, as shown in the figure, is a spherical element representing the engine radiation shield, behind which are the engines and nozzles. The radiation shield is primarily present to block radiation when the engine is firing, but in the current case it can further serve to block radiation when the engine is not firing. We assume that the engine assembly is spherical, is of similar size to the LOX tank, and is located 1 m from the LOX tank. We also assume that the heat shield is composed of bare aluminum on the side facing the LOX tank, but that the open nozzle side may have a fairly high net emissivity, due to the nozzle and engine structures seen from that direction.

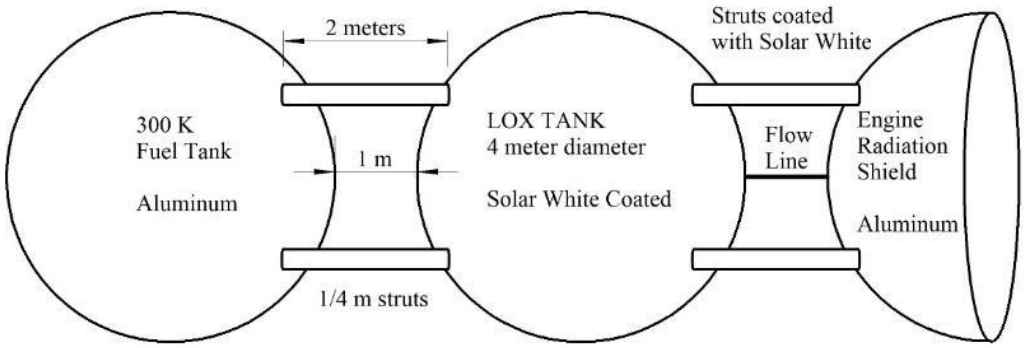

Figure 29. A simplified model of the region around a LOX tank for an Earth-to-Mars vehicle used in the analysis.

It is important to arrive at a reasonable temperature for the engine radiation shield. The highest temperature would be achieved if the Sun were directly illuminating the open end of the engine assembly, heating the engines and nozzles. If we assume that the nozzles and engines have a flat emissivity and can radiate in all directions, they will come to a stable temperature of about 280 K in full sunlight (see Section 1.1). If the radiative shield itself were exposed to the Sun and had a broadband emissivity, it would stabilize at about 330 K (a two-sided plate result).

However, engines and nozzles block some of the sunlight, so an equilibrium temperature of about 300 K for the radiative shield is reasonable. If the sunlight hits the radiative shield directly, i.e. the sunlight comes in from the side of the vehicle, then the engines and nozzles will radiate away their heat and chill, pulling heat from the shield, and keeping it from heating. So again we assume that 300 K is a reasonable steady-state temperature for the heat shield. Of course in our analysis, we assume the engines are not firing since this is the case for most of the time during a trip to Mars.

We assume that the LOX tank is connected to each structure by four 2 m-long, 0.25 m-diameter struts (eight total struts, but only four are shown in the figure). These struts carry the thrust from the engine to the rest of the vehicle and form a framework for the vehicle. It is assumed that there is no additional "skin." In other words, these elements are directly exposed to space and the Sun's irradiance. Finally, we assume a 1 m-long LOX flow line connecting the LOX tank to the engines, passing through the engine heat shield.

One might ask why the engine radiation shield and the fuel tank are not coated with Solar White, and the answer is that Solar White is meant to be placed on objects so that they can passively reach very cold temperatures. That is not the case for the fuel tank or the engine radiation shield. Note that the thermal energy emitted by an aluminum structure at 300 K is low due to the low emissivity of aluminum in the far infrared, whereas the thermal energy emitted by a Solar White coating at 300 K might be substantially larger. So coating these objects with Solar White might result in higher thermal coupling. We do assume the struts are coated with Solar White because they need to passively reach very low temperatures through radiation in order to minimize the heat energy conducted into the LOX tank. These issues will be discussed in more detail in the next sections.

We perform the analysis for only selected Solar White coating materials. One of the goals is to minimize the absorption of radiation from 300 K objects (peaked around 10 μm) and, as is shown in the plots above, KBr does this better than BaF_2. However, the fluorides emit more power than KBr and have a correspondingly larger energy budget. So in most of the following analysis, we will compare the performance of BaF_2 and KBr.

An actual Mars mission vehicle will have a very complicated architecture and a large number of varied thermal emitters and absorbers. But such a vehicle does not yet exist, and even if it did, we do not have the resources to model it. However, the analysis presented below supplies insight and bounds on the primary heat loads affecting the LOX tank, and the general conclusions presented are valid, assuming that a future detailed design does not vary too far from the assumptions stated above.

2.2 Energy Budget

As mentioned above, it would be desirable to be able to keep a LOX tank on a mission to Mars at 80 K in order to reduce the pressure in the tank to 0.03 MPa from the 0.1 MPa needed to keep LOX at 90 K. Using the model developed above, we can calculate the total power emitted from a 1 m-radius LOX tank coated with Solar White at a given temperature. This is then the maximum amount of power that the tank can absorb to not exceed that temperature. The plots in Figure 30 show this power-versus-temperature curve for a 1 m-radius sphere coated with 5 mm of BaF_2, with 10 mm of NaCl, and with 5 mm and 40 mm of KBr.

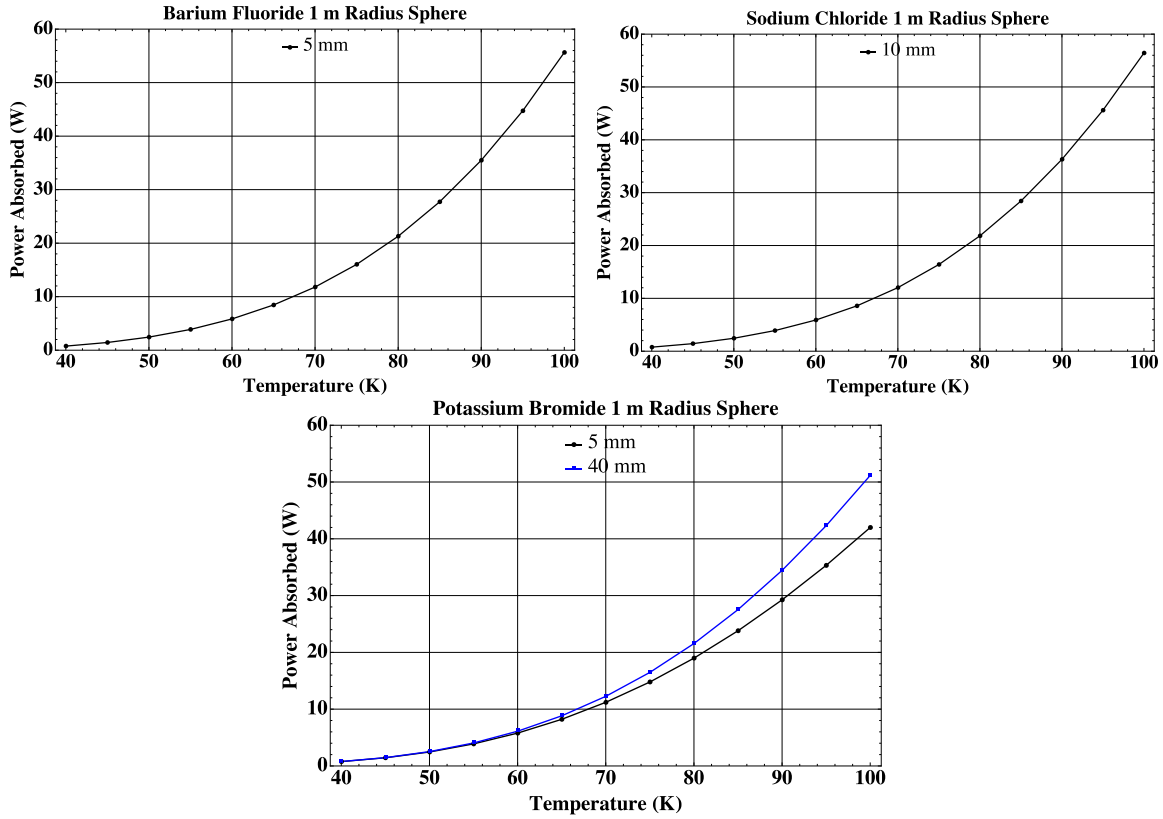

Figure 30. The correspondence between equilibrium temperature and absorbed power for 1 m-radius spheres coated with different types and thicknesses of Solar White.

The first item to point out in these plots is that they do not differ much from one another. This is because the emissivity for these three coatings is similar in the far infrared where the spheres are radiating, so their power-versus-temperature curves, which are essentially an indication of emissivity, are also similar. There is a small difference in the KBr curves with coating thickness because the emissivity cutoff of KBr varies with coating thickness (see the plots above) in a wavelength range where objects at 80 K to 100 K are trying to radiate. The thicker coating has a shorter wavelength transition in emissivity, allowing it to radiate more power at the same temperature.

From the coating thickness plots, a 1 m-radius sphere coated in 5 mm of BaF_2 will absorb about 3.5 W of solar energy and reach a temperature of 53 K. From the plot above, the sphere can absorb another 18 W without exceeding 80 K. Also, since the assumed LOX tank is 2 m in radius, these numbers are four times as large, i.e. a 2 m-radius tank can absorb a total of about 85 W and stay under 80 K when coated with a 5 mm layer of BaF_2. These plots show the available power budget above which either the pressure of the LOX becomes unwieldy or the LOX boils away.

Next, the various additional heat loads will be considered to see what design and location restrictions must be used to stay below these absorbed-energy limits.

2.3 Planetary/Moon IR Heat Load

A potentially large heat contribution to the energy budget is due to the IR emission originating from the Earth, the Moon, or Mars. These entities emit significant amounts of radiation, much of which may be absorbed by the Solar White coating. Recall that the Solar White coating has been designed to reject radiation from the UV through the mid/far-IR region, but the Earth, the Moon, and Mars emit substantial energy in the far-IR to very far-IR bands where the Solar White coating is absorbing. In this section we will discuss the emission from the Earth, the Moon, and Mars and will develop an algorithm to determine the total heat energy absorbed by the LOX tank due to these large entities. We will show that a LOX tank with a Solar White coating cannot be located in a low-altitude orbit, but that at a sufficiently high altitude the additional heat load can be accommodated.

The first step is to develop a thermal emission model for the Earth, for the Moon, and for Mars. The Earth's emission is well known [21] and can be modeled as a perfect blackbody at 255 K. This temperature may seem low, since it is well below the average temperature of the Earth's surface, but the atmosphere acts as a greenhouse material, absorbing radiative energy and reemitting it at colder temperatures, i.e. longer wavelengths. Also, since the atmosphere acts as a heat reservoir, we assume this is the effective emission temperature regardless of time of day.

The Moon has no atmosphere, so we can model it as a blackbody equal to its surface temperature. Since an object in a nonpolar orbit will see a hot, sun-lit side for half an orbit and a dark, cold side for the other half of the orbit, we use two temperatures in our model. We chose to use 396 K for the hot side and 120 K for the cold side.

We assume that the Martian atmosphere has a minimal greenhouse effect; so again, we can use the surface temperatures in our models. We assume a hot side equal to 293 K and a cold side equal to 150 K and chose to model Mars as a blackbody.

Now we need to model the emission from a large sphere, such as the Earth, the Moon, or Mars, that reaches a small sphere, such as a LOX tank on a vehicle in orbit. To do this, we need to develop an irradiance model that couples a large sphere to a small sphere. This is done in the next subsection.

2.3.1 Power Absorbed by a Small Sphere from the Irradiance of a Large Sphere

The goal is to calculate the total power, P_{Ab}, absorbed by a small sphere some center-to-center distance, d, from a large radiating sphere. From our previous work, we know that if parallel radiation with some irradiance spectral density, $I_s(\lambda)$, hits the small sphere, it will absorb an amount of power equal to

$$P_{Ab} = \int_0^{2\pi} \int_0^{\pi/2} \left(\int I_s[\lambda] A[\nu, \lambda] \cos[\nu] \, d\lambda \right) h^2 \sin[\nu] \, d\nu \, d\phi \,,$$

where $A[\nu, \lambda]$ represents the absorption at some differential element on the sphere when radiation arrives at an angle, ν, from normal and wavelength, λ; and h is the radius of the small sphere. We know $A[\nu, \lambda]$ from the work presented above, but we need an expression for $I_s(\lambda)$.

Consider the large radiating sphere, having radius R as shown in Figure 31. The sphere does not produce parallel radiation due to its proximity to the small sphere. However, each differential element on the large sphere can be made small enough that it yields parallel radiation when the radius of the small sphere is very small compared to the distance between the differential element and the small sphere. Since we are concerned with small spheres with radii of a few meters and since these spheres are in orbit (a hundred or more kilometers above the surface of the planet), this condition is met. So the absorbed-power equation above holds for each differential element on the large sphere.

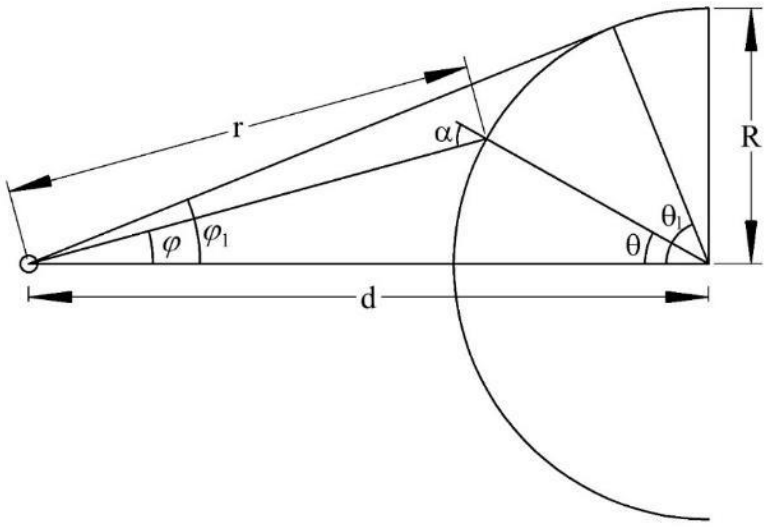

Figure 31. A small sphere near a large sphere.

Since we chose to model the Earth, the Moon, and Mars as blackbodies, we also assume that the differential elements on the large sphere radiate as Lambertian sources. So we start with Planck's law,

$$P_\lambda[\lambda,T]=\frac{2hc^2}{\lambda^5}\frac{1}{\exp[\frac{hc}{\lambda kT}]-1},$$

which provides the radiation emitted from a surface on the large sphere into each wavelength interval and into each solid-angle interval. Since the differential elements and the small sphere are small compared to the distance between them, the solid angle can be replaced with A/r^2, where A is the area in the far field and r is the distance between the differential element and the small sphere (see Figure 31). Using this and the Lambertian assumption, the irradiance at the small sphere from any differential element on the large sphere is given (in watts per meter squared) by

$$dI[\theta,\lambda,T]=\frac{2hc^2}{\lambda^5 r^2}\frac{\cos\alpha}{\exp[\frac{hc}{\lambda kT}]-1}R^2\sin\theta\,d\theta\,d\phi\,.$$

So the total irradiance from the large sphere on the small sphere is obtained by integrating over the large sphere's surface:

$$I_S[\lambda,T]=\int_0^{2\pi}\int_0^{\theta_1}\frac{2hc^2}{\lambda^5 r(\theta)^2}\frac{\cos\alpha(\theta)}{\exp[\frac{hc}{\lambda kT}]-1}R^2\sin\theta\,d\theta\,d\phi\,.$$

This irradiance can be substituted into the first expression above, but there is a hidden assumption here that the small sphere absorbs parallel radiation identically, regardless of the direction to the source of that radiation. We assume the small sphere is uniform across its entire surface, so radiation coming in from different angles can be treated as if it is coming in from one source direction.

In the irradiance expression, the explicit dependences on θ are shown. So to continue, we need the following:

a. θ_1 to set the integration limit,

b. α as a function of the angle θ, and

c. r as a function of θ.

From the law of sines,

$$\frac{\sin(\pi-\alpha)}{d}=\frac{\sin\alpha}{d}=\frac{\sin\varphi}{R}=\frac{\sin\theta}{r},$$

when $\alpha=\pi/2,$ we get

$$\frac{1}{d}=\frac{\sin\varphi_1}{R}=\frac{\sin\theta_1}{r},\ \text{implying that}\ \sin\theta_1=\frac{r}{d},$$

as expected. Now, using the law of cosines,

$$r^2=d^2+R^2-2dR\cos\theta$$

yields a relation for r as a function of θ:

$$r(\theta)=(d^2+R^2-2dR\cos\theta)^{1/2}.$$

Finally, again using the law of cosines,

$$d^2=r^2+R^2-2rR\cos(\pi-\alpha)=r^2+R^2+2rR\cos\alpha.$$

So

$$\cos\alpha=\frac{d^2-r^2-R^2}{2rR}=\frac{-2R^2+2dR\cos\theta}{2rR}=\frac{-R+d\cos\theta}{r}.$$

This shows that

$$\cos\theta_1=\frac{R}{d},$$

again, as expected.

Combining these, we obtain

$$I_S[\lambda,T]=\int_0^{2\pi}\int_0^{\arccos[R/d]}\frac{2hc^2}{\lambda^5(d^2+R^2-2dR\cos\theta)^{3/2}}\frac{(d\cos\theta-R)}{\exp[\frac{hc}{\lambda kT}]-1}R^2\sin\theta\,d\theta\,d\phi.$$

Rearranging, performing the ϕ integral, and dividing the top and bottom by R^3 yields

$$I_S[\lambda,T]=\frac{4\pi hc^2}{\lambda^5\exp[\frac{hc}{\lambda kT}]-1}\int_0^{\arccos[R/d]}\frac{((d/R)\cos\theta-1)\sin\theta}{(1+(d/R)^2-2(d/R)\cos\theta)^{3/2}}d\theta\ .$$

Surprisingly, the θ integral can be done in closed form, yielding

$$I_S[\lambda,T]=\frac{4\pi hc^2}{\lambda^5\exp[\frac{hc}{\lambda kT}]-1}\left(1-\frac{\sqrt{(d/R)^2-1}}{(d/R)}\right).$$

Substituting this expression for the irradiance spectral density into the power expression above yields

$$P_{Ab}=\left(1-\frac{\sqrt{(d/R)^2-1}}{(d/R)}\right)\int_0^{2\pi}\int_0^{\pi/2}\left(\int\frac{4\pi hc^2}{\lambda^5\exp[\frac{hc}{\lambda kT}]-1}A[\nu,\lambda]\cos[\nu]d\lambda\right)h^2\sin[\nu]d\nu d\phi\,.$$

2.3.2 Results for Earth, Moon, and Mars Heat Load on the LOX Tank

The plots in Figure 32 show the results of the model for the Moon. In the left-hand plot, we show the power absorbed as a function of distance from the Moon's center, for both the bright 396 K side and the cold 120 K side. Not surprisingly, the cold side contributes an insignificant heat load, so we have decided to not calculate the cold-side heat contribution for any other case. The left-hand plot shows a 1 m-radius sphere coated with 5 mm of BaF_2, whereas the right-hand side shows a 1 m-radius sphere coated with 5 mm of KBr.

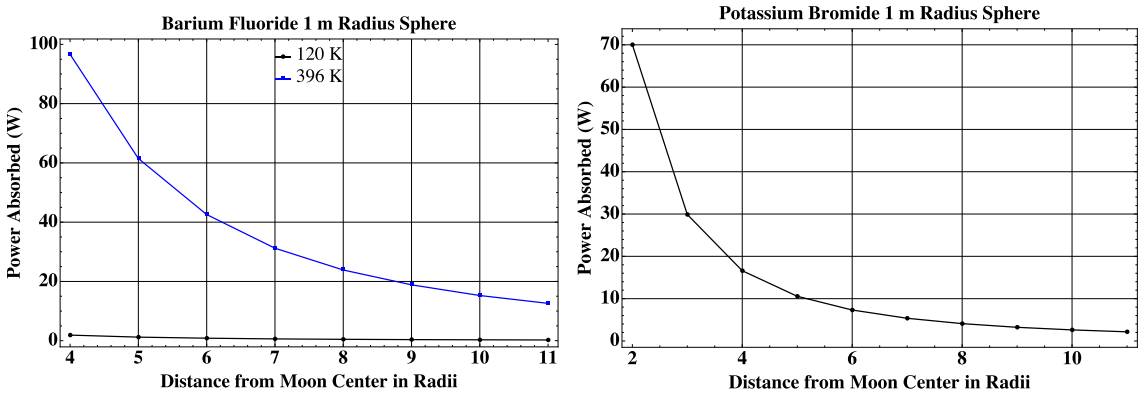

Figure 32. Absorption of power as a function of distance from the Moon's center.

From Wien's law, a 396 K blackbody emits at a peak wavelength of 7.3 µm. For both BaF_2 and KBr, much of this power is not absorbed and is reflected away. But clearly, the BaF_2 absorbs much more than the KBr (see the emissivity curves above and compare BaF_2 and KBr; also, see the average emissivity plot above). Now recall that a 1 m-radius sphere coated with 5 mm of BaF_2 can absorb only 18 additional watts of energy (assuming no other heat contributions), so it cannot come closer than about 6.4 Moon radii from the center of the Moon (recall that the LOX tank will only absorb this power during half of its orbit, so we look for the distance corresponding to 36 W).

The situation for KBr is much better. A 1 m-radius sphere coated with 5 mm of KBr absorbs about 2 W from the Sun, but can only absorb about 19 total watts before the LOX inside exceeds 80 K. So the margin is only 17 W, but due to poor absorption of 396 K radiation by KBr, this means that the LOX tank can get closer (assuming no other heat sources) than 3 Moon radii from the Moon's center (again recall the factor of 2, so we look for the distance corresponding to 34 W on the right-hand plot).

Overall, the Moon is a relatively hot source and it is not possible to maintain a cryogenic LOX tank in a low-altitude orbit about the Moon.

The plots in Figure 33 show the results for the hot side of Mars for the two coatings: 5 mm of BaF_2 and 5 mm of KBr. We are assuming that the cold side of Mars provides insignificant heat, so during a nonpolar orbit, a LOX tank would see the wattage shown below during half the orbit and an insignificant amount of heat during the other half.

Just as it did for the Moon, KBr performs better than BaF_2 due to its longer wave emissivity transition. Also, because Mars is colder than the Moon on its dayside, the heat load is substantially less than for a similar orbit on the Moon. Since a 1 m-radius sphere coated with BaF_2 can absorb 18 W of power, it can absorb 36 W during the hot half of its orbit. And from Figure 33, this means that the LOX tank can be as close as 4.5 Mars radii from the center of Mars, assuming no other heat load. For a KBr-coated sphere, there is a heat margin of 17 W per orbit, or 34 W during the hot half of the orbit. This corresponds to an orbit height of about 2.3 Mars radii from the center of Mars.

The Martian heat load on the LOX tank is lower than for the Moon, but not low enough to allow a low-altitude orbit.

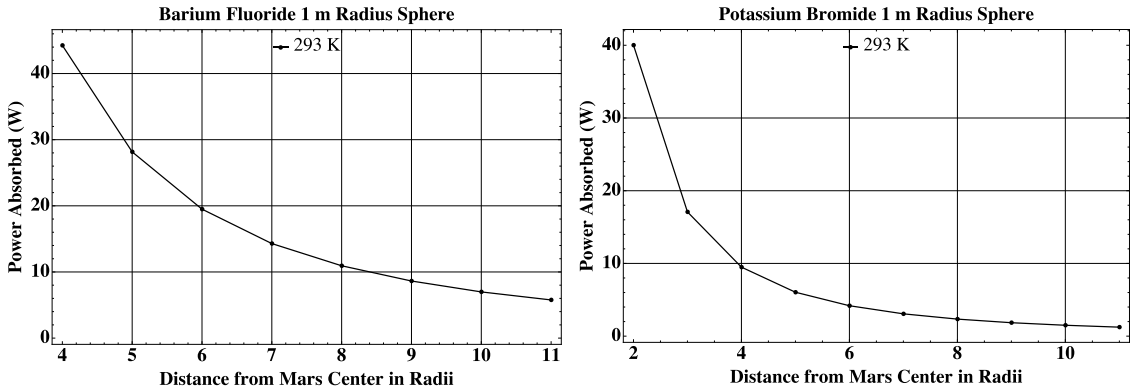

Figure 33. Absorption of power as a function of distance from the center of Mars.

The last case is for the Earth, and the plots are shown in Figure 34. The Earth is cooler than Mars, but it has minimal variation from day to night. So the BaF_2 1 m-radius sphere, which can absorb 18 W of power cannot be closer than about 5 Earth radii from the Earth's center. The KBr 1 m-radius sphere is better and can be as close as about 2.8 Earth radii from the center of the Earth and still keep LOX at 80 K.

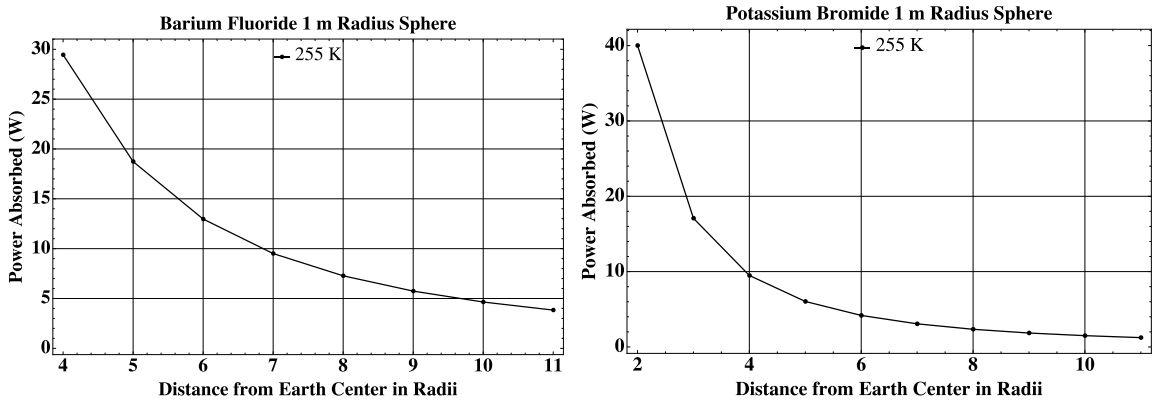

Figure 34. Absorption of power as a function of distance from the center of Earth.

The conclusion is that a Mars mission will not be able to maintain LOX close to the Earth, the Moon, or Mars unless some mitigation is used. These objects emit substantial IR radiation that cannot be adequately rejected by the Solar White coatings. It might be possible to use an IR shield to block this radiation while in orbit and then discard or stow it during the flight. Or, the LOX tank can be filled at a location far from the Earth or the Moon, e.g. one of the Earth-Moon Lagrange points, or at geo, a location about 6.5 Earth radii from the Earth's center. The calculations above assumed that the LOX tank was in full view of the planetary body or the Moon and that the other structures on the vehicle were not shadowing it. In practice, it might be possible to substantially reduce this heat load by aiming the vehicle axis toward the planetary body so that the LOX tank is shadowed.

2.4 Reflected Solar and Planetary Irradiance

The presence of the fuel tank and the engine radiation shield cause both planetary and solar radiation to be scattered/reflected from these two spheres onto the LOX tank, resulting in additional heat absorption. The magnitude of this effect can be approximated by making the following assumptions:

a. Assume that all of the planetary or solar radiation that impinges on the fuel tank or engine radiation shield is scattered uniformly into the 2π radians of half space centered about the axis of the incoming radiation. This is not strictly true. A more accurate model would have the amount of scattered energy vary with the angle between the scattered energy and the incoming radiation and would take into account the surface finish of the fuel tank/shield. However, as long as all of the energy is accounted for in a conservative fashion, such detail is not necessary.

b. Assume that the scattered radiation hitting the LOX tank can be treated as if it were arriving from a distance point. An accurate model would trace the scattered radiation from each location on the fuel tank or shield to each illuminated location on the LOX tank and determine the amount of absorbed power based on the angle the radiation takes with respect to the surface of the LOX tank. However, this would require making surface assumptions on the scatterers (transitioning from specular to diffuse as the wavelengths become long) and would be a cumbersome calculation. By assuming a remote point, the calculation becomes much easier and this assumption is conservative in that it overestimates the heat load. This can be seen by looking at any point on the LOX tank in the field of view of the fuel tank or shield and noting that radiation coming in from a remote point along the vehicle axis hits the LOX tank at an angle closer to normal than the average from the surface of the fuel tank/shield.

Now, the worst case occurs when solar or planetary radiation arrives perpendicular to the vehicle axis. In this case, the LOX tank, fuel tank, and radiation shield are all uniformly illuminated, and no shadowing occurs. The radiation that hits the tank/shield is uniformly scattered into 2π steradians. The LOX tank occupies a total

0.53-steradian solid angle as seen by either the fuel tank or the shield, or 0.27 steradian of the 2π steradians into which radiation is scattered. So about 4.2% of the scattered radiation from either the fuel tank or the radiation shield hits the LOX tank. Now, assuming that this radiation can be treated as originating far away, it can be accounted for by simply increasing the direct radiation load, resulting in an 8.4% increase in the direct solar or planetary irradiance, adding together the contributions from both the fuel tank and the radiation shield. Note that we have implicitly assumed that all of the incoming radiation is scattered by the fuel tank and radiation shield, none is absorbed, in order to maintain conservatism. Even so, this effect is shown to yield a relatively small increase in the LOX tank heat load.

2.5 IR Heat Load on the LOX Tank from Other Vehicle Components

A potentially significant source of heat load on the LOX tank is in the form of IR radiation generated directly by the fuel tank and shield and transmitted onto the LOX tank. To analyze this, consider the fuel tank first, noting that the heat load from the radiation shield will be the same, since it is the same size, material, shape, and distance from the LOX tank as is the fuel tank. Assume for the moment that the fuel tank is perfectly spherical such that its emitted radiation is independent of angle. The LOX tank, as stated above, occupies 0.53 steradian of the fuel tank's field of view, so the LOX tank will intercept 4.2% of the total energy radiated from the fuel tank.

Next, we make an assumption similar to that made above for the reflected irradiance: we assume that the net emissivity of the LOX tank for the 300 K radiation from the fuel tank and shield is equal to the net emissivity for a 300 K aluminum object located in the far field. Again, this a conservative assumption because it causes the irradiance hitting most areas of the LOX tank to arrive closer to normal than if it were arriving from points across the emission area of the fuel tank or radiation shield. Since normal incidence has higher absorption, this assumption will yield an upper bound.

Writing out the formulae, the total power emitted by an aluminum sphere is

$$P_{AlS} = 4\pi R^2 \int_0^{2\pi} d\phi \int_0^{\infty} \int_0^{\pi/2} \frac{2hc^2}{\lambda^5} \frac{\varepsilon_{Al}[\lambda]}{\exp[\frac{hc}{\lambda kT}]-1} \cos[\nu]\sin[\nu]\, d\nu\, d\lambda \,,$$

where $\varepsilon_{Al}[\lambda]$ is the emissivity of aluminum as a function of wavelength, the temperature is assumed to be 300 K, and R is the tank radius (2 m). Then, the average emissivity of LOX tank is given by

$$\langle \varepsilon \rangle = \frac{\int_0^{2\pi}\int_0^{\pi/2}\left(\int \frac{4\pi hc^2 \varepsilon_{Al}[\lambda]A[\nu,\lambda]}{\lambda^5 \exp[\frac{hc}{\lambda kT}]-1}\cos[\nu]\,d\lambda\right)R^2 \sin[\nu]\,d\nu\,d\phi}{\int_0^{2\pi}\int_0^{\pi/2}\left(\int \frac{4\pi hc^2 \varepsilon_{Al}[\lambda]}{\lambda^5 \exp[\frac{hc}{\lambda kT}]-1}\cos[\nu]\,d\lambda\right)R^2 \sin[\nu]\,d\nu\,d\phi}$$

$$= \frac{2\pi\int_0^{\pi/2}\left(\int \frac{4\pi hc^2 \varepsilon_{Al}[\lambda]A[\nu,\lambda]}{\lambda^5 \exp[\frac{hc}{\lambda kT}]-1}\cos[\nu]\,d\lambda\right)\sin[\nu]\,d\nu}{\pi\left(\int \frac{4\pi hc^2 \varepsilon_{Al}[\lambda]}{\lambda^5 \exp[\frac{hc}{\lambda kT}]-1}\,d\lambda\right)} = \frac{2\int_0^{\pi/2}\left(\int \frac{\varepsilon_{Al}[\lambda]A[\nu,\lambda]}{\lambda^5 \exp[\frac{hc}{\lambda kT}]-1}\cos[\nu]\,d\lambda\right)\sin[\nu]\,d\nu}{\left(\int \frac{\varepsilon_{Al}[\lambda]}{\lambda^5 \exp[\frac{hc}{\lambda kT}]-1}\,d\lambda\right)}.$$

Then the power absorbed by the LOX tank from the fuel tank or from the radiation shield can be conservatively estimated to be $\langle \varepsilon \rangle\, 0.042\, P_{AlS}$.

In order to calculate the power emitted by a spherical tank, P_{AlS}, an emissivity for aluminum is needed. For the moment assume that the aluminum on the fuel tank and radiation shield is a bare, nonfinished aluminum surface. In this case, in the infrared, a reasonable emissivity is about 0.1 for all wavelengths of interest [22]. If we make this assumption the total power emitted by a 2 m-radius tank is 2300 W. In addition, since the emissivity is assumed to be wavelength-independent, the average emissivity can be obtained from the average emissivity plot provided a few pages back. Combining these results, we can determine the total power absorbed by the LOX tank from the IR radiation emitted by the fuel tank or radiation shield.

If the LOX tank is coated with Solar White consisting of 5 mm of KBr, then its average emissivity at 300 K is 0.109 and the absorbed power due to either the fuel tank or the radiation shield is 10.5 W, i.e. 21 W total for both IR emitters.

If the LOX tank is coated with Solar White consisting of 5 mm of BaF_2, then its average emissivity at 300 K is 0.518 and the absorbed power due to either the fuel tank or the radiation shield is 50 W, i.e. 100 W total for both IR emitters.

2.6 Conduction Along a Solar White-Coated Strut and Feed Line

The various heat loads analyzed previously have all been radiative in nature; however, by some accounts the most significant heat load to a cryogenic tank in space is not radiative, but conductive [23]. In this section of the report, we will show that by coating a strut with Solar White, it may be possible not only to prevent heat flow to the LOX tank along a strut, but even to pull some heat from the tank. The reason for this is that a Solar White-coated cylinder, as shown in the previous sections, can become very cold, even in the presence of the Sun. When warm, such a cylinder will radiate more energy than it absorbs, causing it to cool down.

To analyze this effect, we consider the hollow cylinder shown in Figure 35. We decompose the cylinder into a large number of thin rings of width dx, and number these with the index i. Assume that the temperature of each ring is uniform around the ring (i.e. the time scales are long enough that the small amount of solar heating distributes itself around the ring), that one end of the cylinder is attached to a 300 K object (the fuel tank or engine radiative

shield), and that the other end is attached to the LOX tank. In steady state, the temperature of each ring is constant, so the energy entering the ring must equal the energy leaving the ring. This energy equation is expressed as

$$k[(T[i-1]+T[i])/2]\frac{\pi r_i^2-\pi r_o^2}{dx}(T[i-1]-T[i])-k[(T[i]+T[i+1])/2]\frac{\pi r_i^2-\pi r_o^2}{dx}(T[i]-T[i+1])+P_{Sol}[i]-P_{Rad}[i]=0,$$

where $k[T]$ is the thermal conductivity of the cylinder material as a function of temperature, r_i is the cylinder inner radius, r_o is the cylinder outer radius, $P_{Sol}[i]$ is the solar power absorbed by the ring, and $P_{Rad}[i]$ is the thermal radiation emitted by the ring.

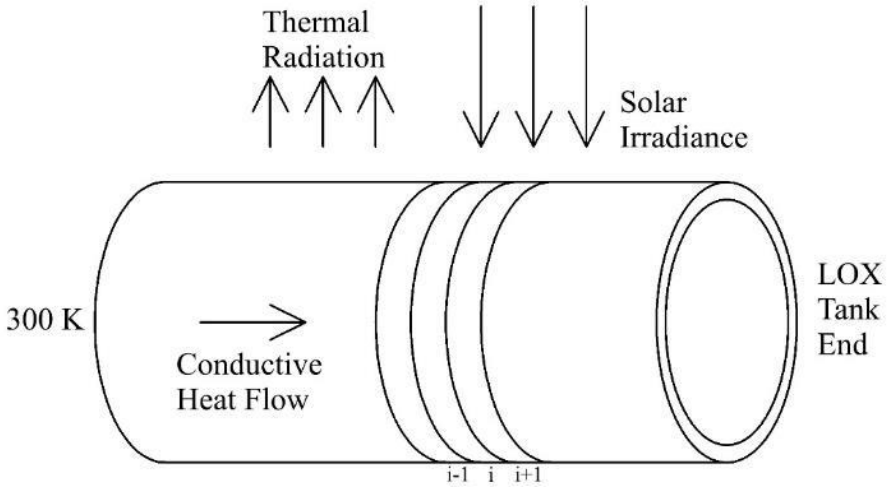

Figure 35. The energy routes for a hollow tube, such as a strut, connecting a 300 K object to the LOX tank.

Before proceeding, a comment is needed on the thermal conductivity as a function of temperature, $k[T]$. Several references from before 1980 show the thermal conductivity of most metals increasing as temperature is lowered. However, a more recent reference from NIST [24] shows the thermal conductivities decreasing with temperature. The discrepancy between these published results is large and can affect our results, with the more recent publication yielding less heat flow along the cylinder. We have decided to use these more recent results, not because they help further the benefits of the Solar White coating, but because the more recent publication is directed at specific alloys of metals and is more recent, so we believe it is more accurate.

We chose three cylinder materials to study: aluminum, stainless steel, and titanium. Wesley Johnson of the Glenn Research Center (GRC) calculated wall thicknesses for the cylinders. Assume that they were 2 m long and had an outer diameter of 0.25 m. For aluminum 6061 he calculated 8.2 mm, for stainless steel 316 he calculated 7.1 mm, and for titanium he calculated 2.4 mm. He assumed a safety factor of 1.4 and a load of 220 kN per strut and calculated the wall thickness based on the onset of local buckling.

We modeled three materials with two different Solar White coatings: 5 mm of BaF_2 and 5 mm of KBr (we also still assume a thin layer of silver under the scattering layer) on aluminum 6061 T6, stainless steel 304, and titanium Ti-6Al-4V (slightly different alloys than used for the wall thickness measurements). In each case we divided the strut into 200 small rings, yielding 200 linear equations for the temperature. We assumed a 300 K boundary condition at one end of the strut and an 80 K boundary condition at the other end. Mathematica was used to solve the coupled equations, and the results are plotted in Figure 36.

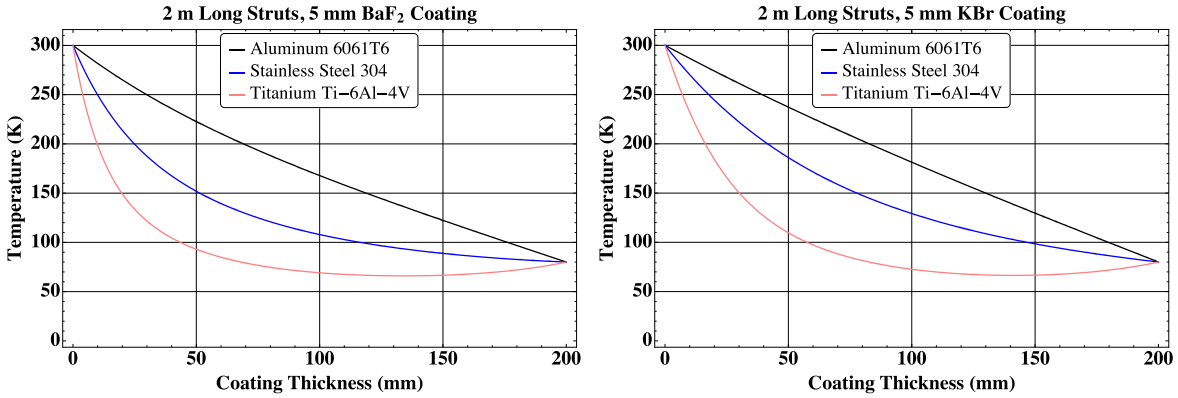

Figure 36. The temperature profile of a 2 m-long, 0.25 m-diameter strut of different materials with two different Solar White coatings, assuming an 80 K cold boundary.

The aluminum cylinder has a relatively thick wall and the highest thermal conductivity of the three materials, resulting in substantial thermal power entering the LOX tank (note the large negative slope at the end of the aluminum plots). Calculations show 44.7 W of heat for the BaF_2 and 52.6 W of heat for the KBr entering the LOX tank along each strut. The difference between the two coatings is due to the significantly higher IR emittance of the BaF_2 causing it to lose heat to radiation more quickly than for the KBr. However, the thermally radiated power for either case is small compared to the conducted power. Clearly, using aluminum struts would prevent the long-term storage of LOX.

Next, consider the results for stainless steel. The stainless-steel strut still has relatively thick walls, but the thermal conductivity of stainless steel is much less than for aluminum. So the conducted heat power is less and the thermally radiated power has more effect on the temperature along the cylinder. The BaF_2 strut temperature profile drops faster than the KBr cylinder, so the slope at the end of the strut, which determines the power entering the LOX tank, is smaller. Numerically, 0.47 W of heat flow into the LOX tank with the BaF_2-coated cylinder and 1.3 W flow into it for the KBr-coated cylinder.

Finally, consider the titanium cylinder. Titanium has a thermal conductivity similar to stainless steel, but the wall of the titanium cylinder is less than 1/3 the thickness of the stainless-steel cylinder. So now the thermally radiated power is the dominant effect over the conducted heat power. Note that the temperature plot for the BaF_2-coated cylinder still drops faster than the temperature plot for the KBr-coated cylinder, but now both cylinders emit so much thermal power that they achieve temperatures lower than 80 K, the temperature of the LOX tank. So the coated titanium struts actually pull heat power away from the LOX tank. The BaF_2-coated strut pulls 0.346 W out and the KBr cylinder pulls out 0.351 W, slightly more because it reaches a lower temperature along its length than the BaF_2-coated strut does.

Since the titanium-coated struts reach temperatures less than 80 K, we decided to model the struts with a 60 K LOX tank boundary condition. The resulting plots are shown in Figure 37.

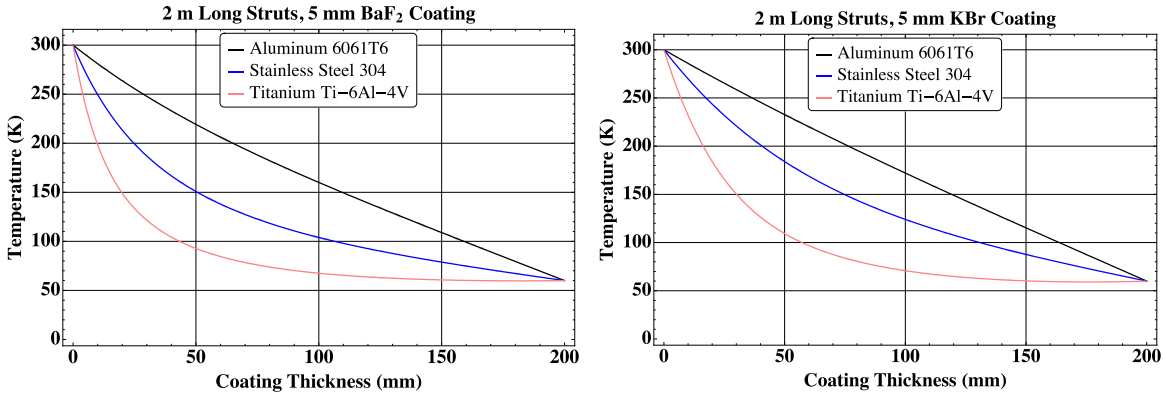

Figure 37. The temperature profile of a 2 m-long, 0.25 m-diameter strut of different materials, with two different Solar White coatings, assuming a 60 K cold boundary.

All of the comments made above still hold. The temperature along the aluminum strut is dominated by heat conduction, the temperature profile for the stainless-steel strut is dictated by both conductive and radiated power, and the temperature profile for the titanium strut is dictated by radiated power. Numerically, the BaF_2-coated strut with a 60 K boundary causes 43.2 W to enter the tank when composed of aluminum, 1.29 W when composed of steel, and −0.016 W when composed of titanium. The KBr-coated strut with a 60 K boundary causes 48.8 W to enter the tank when composed of aluminum, 1.88 W when composed of steel, and −0.042 W when composed of titanium.

Summarizing the above results, stainless-steel struts would allow the long-term storage of LOX, but clearly, titanium struts are preferable. Titanium struts result in no net heat flow to the LOX tank under our assumptions and are relatively thin and lightweight. The only significant negative is stress induced by relative thermal contraction between the LOX tank (likely composed of aluminum) and welded titanium struts.

Sadly, the feed line connecting the LOX tank to the engine must be made of aluminum since it is a thin wall line meant to carry LOX. Wesley Johnson at GRC has stated that the feed line should be 75 mm in diameter and have a wall thickness between 1 mm and 3 mm. The plots in Figure 38 show the results of our model for the 3 mm-wall-thickness feed line demonstrating, just as with the struts, that heat conduction dominates radiative emission in this case. As above, the slope of these curves at the cold end determines the net power flow into the tank. For the BaF_2 case, it is about 10 W, and for the KBr case it is about 11 W.

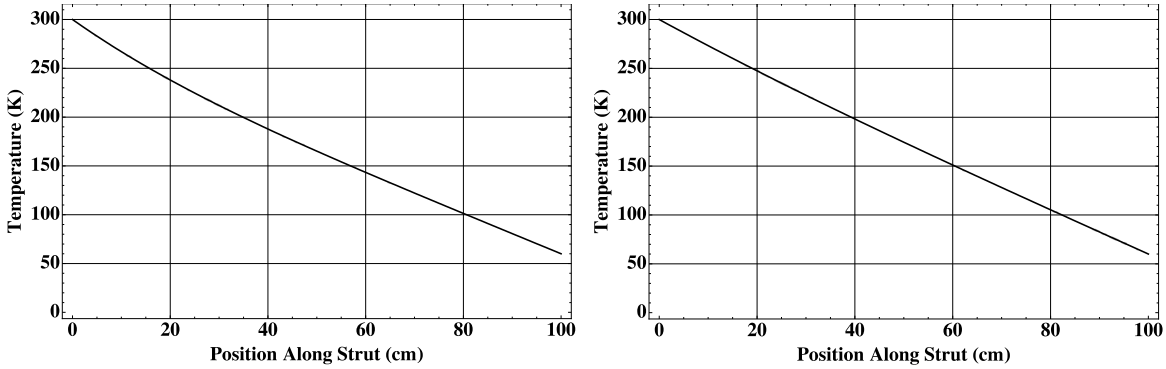

Figure 38. The temperature profile for an aluminum feed line with 3 mm wall thickness connecting the LOX tank to the engines. The left plot is for 5 mm of BaF_2, and the right plot is for 5 mm of KBr.

Because these heat loads are high, we decided to model the Solar White-coated fuel line assuming 1 mm walls in order to decrease the conducted heat. The results are shown in the plots in Figure 39.

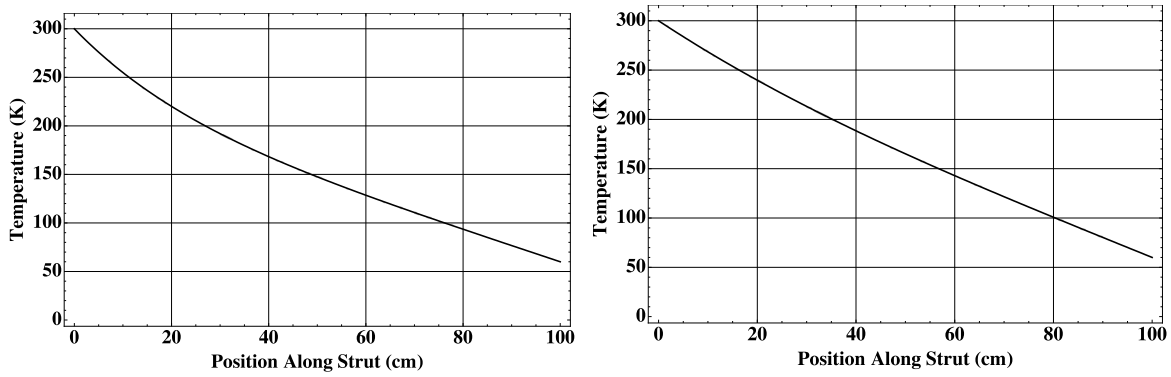

Figure 39. The temperature profile for an aluminum feed line with 1 mm wall thickness connecting the LOX tank to the engines. The left plot is for 5 mm of BaF_2, and the right plot is for 5 mm of KBr.

The power flow into the LOX tank using 1 mm wall thickness for the feed line is 2.8 W for the BaF_2-coated line and 3.3 W for the KBr-coated line. In the analysis below, we will use the results for the 1 mm wall thickness and round them, stating that both coatings cause 3 W of conducted thermal power to enter the LOX tank along the feed line.

2.7 Total Heat Load and Conclusions

2.7.1 Proposed Design

Summarizing the situation, a 4 m-diameter LOX tank coated with 5 mm of BaF_2 Solar White or 5 mm of KBr can absorb only about 84 W of energy and stay below 80 K (24 W and stay below 60 K). These values are obtained from the energy budget plots and multiplying the numbers shown by 4 to account for the LOX tank having a 2 m radius. From Table 2, a 2 m-radius LOX tank coated with BaF_2 Solar White will absorb about 13.5 W of solar energy and a 2 m-radius LOX tank coated with KBr Solar White will absorb about 8.3 W.

So there is some margin to work with; however, the radiated heat load from the fuel tank and the engine radiation shield were shown to be 100 W for a BaF_2-coated LOX tank and 21 W for a KBr-coated LOX tank. This rules out the BaF_2 Solar White-coated tank and increases the total heat load on the KBr-coated LOX tank to about 29.3 W.

We've shown that the heat load due to the struts can be reduced to zero by using titanium, but the heat load due to the fuel line will be about 3 W. Also, we showed that the solar radiation heat load is increased by 8% due to scattering off of the fuel tank and the engine radiation shield (this is an additional 0.7 W). So the total heat load on the KBr-coated LOX tank is about 33 W (ignoring planetary radiation). Looking at the energy budget plots, 8 W on a 1 m-radius tank corresponds to a stable temperature of 65 K, so 33 W on a 2 m-radius LOX tank will also yield an equilibrium temperature close to 65 K. This is a positive result since it indicates that not only can LOX be maintained on a trip to Mars, but it can be maintained at a low enough temperature that the pressure within the LOX tank is very low. Of course, this result assumes no planetary IR heat load.

2.7.2 Alternative Design

It has been shown that if titanium struts are used, the largest heat load contribution on the LOX tank is due to radiative coupling with the fuel tank and the engine radiation shield. It could also be argued that we did not include this source of radiation in our strut analysis and that including it would increase the heat load to the struts and to the LOX tank.

One way to circumvent both of these issues is to modify the vehicle design and install thin, highly reflective metallic radiation shields between the LOX tank and the other two vehicle elements, as shown in Figure 40.

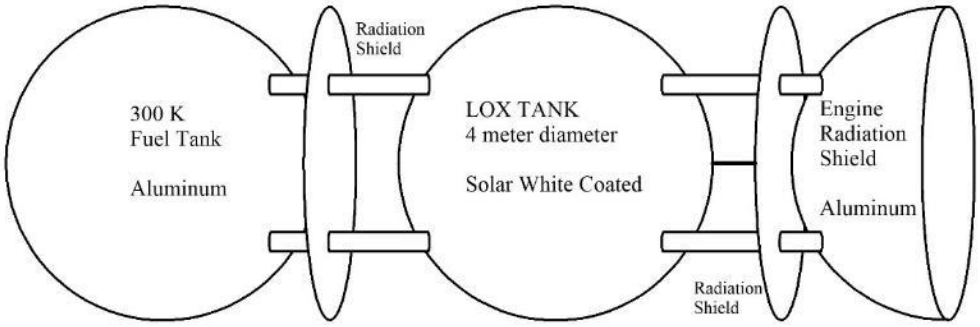

Figure 40. The Mars vehicle with radiation shields.

Installing these radiation shields will significantly lower the IR heat load on the LOX tank and the struts for two reasons. First, the radiation shields will come to an equilibrium temperature lower than 300 K. From multilayer insulation theory [25], the temperature of the radiation shield to the fourth power will be roughly the weighted average of the temperatures of the LOX tank, the 300 K elements, and microwave background of the universe raised to the fourth power. The weighting is determined by the field of view of the radiation shield. Assuming conservatively that the radiation shield sees a 300 K element in 1/3 of its field of view (the LOX tank and microwave background contribute a negligible amount due to their relatively low temperatures), then the radiation shield equilibrium temperature will be about 230 K. Second, the radiation shields can be made highly reflecting so that, conservatively, an emissivity of 0.02 can be assumed. The consequence of these two effects is that the radiation shield will lower the IR heat load on the LOX tank by a conservative factor of 10 (15 scaled down to 10 to account for the increase in emissivity of the LOX tank coatings at lower temperature). In other words, the BaF_2-coated LOX tank will now only see about 10 W of IR heat load and the KBr-coated LOX tank will see about 2 W of heat load.

With the radiation shields, the scattered solar radiation is also blocked, and the titanium struts are shielded from IR heat load as well. Consequently, the total heat load on the BaF_2-coated tank is now 13.5 W from the Sun, 10 W from the radiation shields, and 3 W from the fuel line, summing to 26.5 W. This corresponds to a steady-state temperature of 63 K! The KBr tank receives 8.3 W from the Sun, about 2 W from the radiation shields, and 3 W from the fuel line, summing to 13.3 W. This corresponds to a steady-state temperature of about 55 K! Using radiation shields lowers the heat load on the LOX tank and reduces its temperature, allowing more leeway for other heat sources and allowing thinner tank walls.

Before leaving this section it should be mentioned that on a trip to Mars the vehicle might travel near the Sun, even somewhat within the orbit of Venus. If we assume that the vehicle may pass within 0.6 AU of the Sun, the solar irradiance could be three times as high as it is at 1 AU. This would increase the solar heat load on the BaF_2-coated LOX tank from 13.5 W to 40.5 W and on the KBr-coated LOX tank from 8.3 W to 25 W. Without the extra radiation shields, the KBr LOX tank would now rise from 33 W total heat load to about 50 W and reach a steady-state temperature a little above 70 K. With the additional radiation shields, the BaF_2-coated tank would have a total heat load of 53.5 W and a steady-state temperature of a little above 70 K; and the KBr-coated tank would

have a total heat load of 30 W and a steady-state temperature of about 63 K. All of these results indicate that LOX can be maintained even when passing this close to the Sun for long periods.

As a final word of warning, if a KBr-coated LOX tank is used with the extra radiation shields, as the Mars vehicle moves away from the Sun the solar heat load can drop by more than a factor of 2. So the total heat load on the KBr-coated LOX tank could drop to as low as 9 W, resulting in a steady-state temperature for the LOX tank that could drop below 50 K. Since LOX freezes at 50 K, this could pose a mission problem.

3. OTHER SOLAR WHITE APPLICATIONS

We have only begun to explore the other applications for this new cryogenic selective surface, but a partial list would include the following:

a. A coating for a deep-space LOX or LN_2 tank or other cryogenic tank, allowing liquid or even solid cryogenic commodities to be stored in a depot in the presence of the Sun at locations less than 1 AU from the Sun.

b. A coating for LH_2 tanks. Even though the above designs can't achieve the temperatures of LH_2 (around 20 K at 1 atm), they will dramatically reduce the solar and conductive heat loads on the LH_2, thereby preserving it for much longer periods.

c. A coating for liquid-methane tanks, which would require temperatures between 90 K and 110 K.

d. Coatings to maintain LOX or LN_2 on the Moon, where background thermal radiation, conductivity, and solar radiation are all present.

e. A coating for elements in addition to struts to help minimize the transfer of heat from warm elements to cryogenic elements.

f. A better heat shield for reaching cold temperatures for sensors and low-temperature experiments. Heat shields, or solar shields, are currently used to reduce the heat load on space items that require cooling, such as the James Webb telescope. Designers are currently limited to using existing thermal control coatings designed to radiate in the mid to far infrared, i.e. materials designed for rejecting heat from a 300 K object, to try and achieve low temperatures in space, an application they were not designed to meet. Solar White is a coating designed to reach and operate optimally at very cold temperatures.

g. A coating for superconducting wire, allowing superconducting operation in deep space without the need for a refrigeration system.

   (1) This would allow efficient power transmission.

   (2) This would allow superconducting magnets to be used in space.

   (3) This might enable the construction of an active radiation shield against galactic cosmic radiation.

h. A way to allow missions to approach much closer to the Sun than with other coatings. Such an application needs verification since this would not be a cryogenic use, but is a fascinating possible advance resulting from this technology.

It should be recalled that these coatings are not meant to emit heat, but to maintain a cold temperature. They are not a replacement for currently available thermal control coatings, but a new type of coating allowing cryogenic temperatures to be reached and maintained. The new Solar White coating meets a need that no other coating meets and should enable the long-term storage of cryogens in deep space and the passive operation of superconductors in deep space.

4. SUMMARY

A coating has been described and modeled that can reject significantly more sunlight in space than any currently available coating (see also [26]). The best available thermal control coatings, or selective surfaces, are stated in the literature as absorbing 7% of the Sun's energy, whereas these new Solar White diffusive coatings have achieved, theoretically, less than 0.1% solar energy absorption. These new coatings are composed of materials that are transparent to most of the solar spectrum and include MgF_2, CaF_2, BaF_2, CsBr, KCl, NaCl, and KBr, as well as others. If these materials are used to create a diffusive material, then they will scatter the solar energy, not absorb it, and will prevent most of it from propagating through the coating in a process similar to how white paint works in the visible portion of the spectrum. The majority of the Sun's energy will be backscattered, not absorbed, resulting in very low net absorption of energy. This effect can be enhanced by placing a metallic reflector behind the diffusive coating so that long-wave solar radiation, which would not be scattered by the small particles making up the coating, will also be reflected and not absorbed.

Applying these coatings to plates, cylinders, and spheres, and then virtually placing them at 1 AU from the Sun and modeling their performance has yielded cryogenic equilibrium temperatures. This is an enabling result in that no previous coating allows cryogenic temperatures to be achieved. With these new coatings, it may now be possible to store cryogenic commodities, such as LOX and LN2, in deep space, and it may now be possible to operate superconducting wires in deep space without a refrigeration system. It might even be possible to freeze oxygen or nitrogen in space.

We have developed a simplified model of a Mars vehicle containing a LOX tank held between two 300 K spheres, one representing an engine radiation shield and the other a fuel tank. We modeled the solar radiation scatter off of these two elements and the IR heat emitted by them onto the LOX tank, as well as the conducted heat load along support struts and a fuel line. Summing these, we showed that a 5 mm coating of KBr-based Solar White was able to maintain the LOX even in the presence of these heat loads. We then showed that by adding two more radiation shields (one between the LOX tank and each of the two 300 K-emitting spheres), the heat loads could be reduced substantially. This both reduced the temperatures and would allow a Solar White coating based on BaF_2 to be used to maintain LOX on a long-duration Mars mission. We calculated the IR heat load from the Earth, Mars, and the Moon and showed that the vehicle must not enter a low-altitude orbit unless a shield or shadowing is used to reduce the IR radiation from the body being orbited. We also listed several additional possible uses for Solar White coatings.

Significant experimental work remains to be performed, including verifying our models, constructing the proposed coatings, and testing them in a simulated space environment; and we hope to obtain funding to do this.

5. REFERENCES

1. C.G. Granqvist, "Radiative heating and cooling with spectrally selective surfaces," *Applied Optics* **20**(15):2606−2615 (Aug 1, 1981) (A short review article with 349 references).
2. J.H. Henninger, "Solar Absorptance and Thermal Emittance of Some Common Spacecraft Thermal-Control Coatings," NASA Reference Publication 1121 (Apr 1984).
3. D.F. Hall and A.A. Fote, "Thermal Control Coatings Performance at Near Geosynchronous Altitude," *J. of Thermophysics and Heat Transfer* **6**(4):665−671 (Oct−Dec 1992).
4. "Spacecraft Thermal Control and Conductive Paints/Coatings and Services Catalog," AZ Technology, Huntsville, AL (Jan 2008).
5. A.P. Raman, M.A. Anoma, L. Zhu, E. Rephaeli, and S. Fan, "Passive radiative cooling below ambient air temperature under direct sunlight," *Nature* **515**(7528):540−544 (Nov 27, 2014).

6. L. Zhu, A.P. Raman, and S. Fan, "Radiative cooling of solar absorbers using a visibly transparent photonic crystal thermal blackbody," *Proc. of the National Academy of Sciences* **112**(40):12282−12287 (Oct 6, 2015).
7. R.R. Hibbard, "Equilibrium Temperatures of Ideal Spectrally Selective Surfaces," *Solar Energy* **5**(4):129−132 (Oct−Dec 1961).
8. *Handbook of Optical Constants*, ed. Edward D. Palik, 5 vols, San Diego, CA: Academic Press (1997).
9. www.crystran.com.uk/optical-materials.
10. G.B. Irani, T. Huen, and F. Wooten, "Optical constants of silver and gold in the visible and vacuum ultraviolet," *JOSA* **61**(1):128−129 (1971).
11. M.A. Ordal, L.L. Long, R.J. Bell, S.E. Bell, R.R. Bell, R.W. Alexander, and C.A. Ward, "Optical properties of the metals al, co, cu, au, fe, pb, ni, pd, pt, ag, ti, and w in the infrared and far infrared," *Applied Optics* **22**(7):1099−1119 (1983).
12. L.G. Schulz, "The optical constants of silver, gold, copper, and aluminum, I. The absorption coefficient k," *JOSA* **44**(5):357−362 (1954).
13. S. Chandrasekhar, *Radiative Transfer*, New York: Dover (1960).
14. Arthur Schuster, "Radiation through a foggy atmosphere," *The Astrophysical Journal* **21**:1 (1905).
15. Dupont document, DuPont™ Ti-Pure® titanium dioxide, Titanium Dioxide for Coatings, https://www.chemours.com/Titanium_Technologies/en_US/tech_info/literature/Coatings/CO_B_H_65969_Coatings_Brochure.pdf.
16. J.R. Howell, R. Siegel, and M.P. Menguc, *Thermal Radiation Heat Transfer*, 5th ed., Boca Raton, FL: CRC Press (2010).
17. D. Zhang, E. Cherkaev, and M.P. Lamoureux, "Stieltjes representation of the 3D Bruggeman effective medium and Padé approximation," *Applied Mathematics and Computation* **217**(17):7092−7107 (May 1, 2011).
18. M. Born and E. Wolf, *Principles of optics: electromagnetic theory of propagation, interference and diffraction of light*, Cambridge Press (1999).
19. J. DeKruif and B.F. Kutter, "Centaur upperstage applicability for several day mission durations with minor insulation modifications," *Joint Propulsion Conference*, AIAA-2007-5845, Hartford, CT (2007).
20. W.L. Johnson, S.G. Sutherlin, and S.P. Tucker, "Cryogenic propellant insulation system design tools for mass optimization of space vehicles," *SPACE*, pp. 9−11 (2008).
21. J. Harries, B. Carli, R. Rizzi, C. Serio, M. Mlynczak, L. Palchetti, T. Maestri, H. Brindley, and G. Masiello, "The far-infrared Earth," *Reviews of Geophysics* **46**(4) (2008).
22. Chang-Da Wen and Issam Mudawar, "Modeling the effects of surface roughness on the emissivity of aluminum alloys," *International Journal of Heat and Mass Transfer* **49**(23):4279−4289 (2006).
23. Edgar R. Canavan and F.K. Miller, "Optimized Heat Interception for Cryogen Tank Support" (2007).
24. E.D. Marquardt, J.P. Le, and Ray Radebaugh, "Cryogenic material properties database," in *Cryocoolers 11*, pp. 681−687, Springer US (2002).
25. Robert C. Youngquist, Mark A. Nurge, Wesley L. Johnson, and Stanley O. Starr, "Modeling Transmission Effects on Multilayer Insulation," *Journal of Thermal Science and Engineering Applications* **7**(2):021007 (2015).
26. Robert C. Younquist and Mark A. Nurge, "Achieving cryogenic temperatures in deep space using a coating," *Optics Letters* **41**(5):TBD (2016).